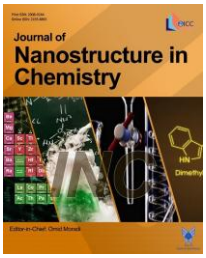

J. Nanostruct Chem. 2026; 16(4): 332-354

Journal of Nanostructure in Chemistry (JNSC)

https://doi.org/10.57647/jnsc.2026.1604.17

Research Article

Machine Learning and Quantum-Inspired Optimization of Microwave-Synthesized High-Entropy Alloy Magnetic Nanoparticles for Photocatalytic Diazinon Degradation

Mostafa Khajeh[1,2,*], Mansour Ghaffari-Moghaddam[1,2,*], Jamshid Piri[2,3,*], Afsaneh Barkhordar[1]

[1]*Department of Chemistry, Faculty of Science, University of Zabol, Zabol, Iran*
[2]*Advanced Materials & Manufacturing Laboratory, University of Zabol, Zabol, Iran*
[3]*Department of Water Engineering, Faculty of Water and Soil, University of Zabol, Zabol, Iran*

*Corresponding authors: m_khajeh@uoz.ac.ir , mansghaffari@uoz.ac.ir , j.piri@uoz.ac.ir

Article History:

Received:
17 December 2025

Revised:
15 February 2026

Accepted:
07 April 2026

Published in Issue:
31 August 2026

Abstract

This study reports the synthesis of high-entropy alloy-functionalized magnetic nanoparticles (HEA@MNP) photocatalysts and investigates their application for the photocatalytic degradation of diazinon pesticide under visible LED irradiation. The core-shell nanoarchitecture of Fe_3O_4 magnetic core and Co-Ni-Cu-Zn-Mn HEA-like shell was prepared using a co-precipitation method combined with a microwave-assisted functionalization technique. FTIR, SEM-EDX, PXRD, and TG did characterization of HEA@MNP. The HEA@MNP photocatalysts exhibited excellent photocatalytic activity with a high degradation efficiency of 97.4% for diazinon, good adsorption capacity of 169.5 mg/g, and excellent reusability retaining 93% retained efficiency after seven cycles without noticeable emission of heavy metal ions. For process modeling and optimization, a full-fledged machine learning framework with four algorithms (LSTM-XGBoost, Gaussian Process, Polynomial Ensemble, and Ultimate Ensemble) was established. Among the evaluated models, the Ultimate Ensemble achieved the highest test R^2 of 0.936; however, overfitting analysis (ΔRMSE% = 49.5%) revealed moderate model instability. The Polynomial Ensemble demonstrated the most robust generalization performance (ΔRMSE% = 7.7%, Generalization Score = 0.969), suggesting it may be more reliable for practical applications despite slightly lower test metrics. For the multi-objective optimization, a new quantum-inspired genetic algorithm (QGA) was designed, and it has proven to be very effective in the solution processes with computational efficiency compared to the traditional methods (31 iterations are needed to converge instead of 300). Application of the QGA optimization approach enabled a 21.6% reduction in catalyst loading while sustaining a degradation efficiency of 86.48%, thereby enhancing the overall cost-effectiveness of the process by approximately 28.5%, Herein, photocatalytic scavenging experiments were carried out and showed that holes generated during the irradiation process are responsible for the predominant oxidation, and hydroxyl/superoxide radicals are the secondary oxidants. This combination of advanced materials, machine learning, and quantum-inspired optimization represents an elegant platform for sustainable water treatment technologies.

Keywords: Diazinon; High-entropy alloy; Quantum genetic algorithm; Machine learning optimization; Photocatalytic degradation

Cite this article: Khajeh M., Ghaffari-Moghaddam M., Piri J., Barkhordar A. Machine Learning and Quantum-Inspired Optimization of Microwave-Synthesized High-Entropy Alloy Magnetic Nanoparticles for Photocatalytic Diazinon Degradation. *J Nanostruct Chem* 16, 332-354 (2026). https://doi.org/10.57647/jnsc.2026.1604.17

1. Introduction

Chemical pesticides are a broad category of chemicals intended to kill insects, weeds, and disease-causing agents. However, being environmentally persistent and toxic in nature, they cause significant harm to human health and natural ecosystems [1, 2]. One of them, diazinon ($C_{12}H_{21}N_2O_3PS$), is an extensively used organophosphate pesticide with high toxicity, employed in agricultural practices, animal treatment, and domestic pest control [3]. Despite regulatory restrictions in the United States and the European Union, diazinon is still in common global use [4, 5]. The compound is introduced into aquatic systems by farm runoff, precipitation, and factory release, and is toxic to aquatic organisms at levels as low as 350 ng/L [6]. Traditional elimination techniques—such as sorption, flocculation, membrane filtration, biodegradation, and chemical treatment—are energy-intensive, chemical-dependent, and frequently ineffective, in addition to being capable of producing toxic secondary products or waste streams [7-9]. Because of diazinon's stability and toxicity, there is still research being conducted to find safer and more effective treatment techniques. As a result of this, photocatalytic treatments have emerged as green techniques utilizing illumination energy to degrade diazinon into less toxic or non-toxic products, and maybe even complete mineralization.

The application of nanoscience is rapidly advancing and has become integral to many aspects of daily life. Nanoparticles (NPs) have proved to be highly efficient for pollutant degradation and organic pollutants from wastewater [10, 11]. Among these, magnetic nanoparticles (MNPs) are especially useful in that they possess a nanometer size, magnetism, low toxicity, chemical inertness, ease of synthesis, surface modification, bioactivity, and easy separation. In addition, the magnetic material is the most important one, since they are easily recoverable from treated water through an external magnetic field, thus making it reusable as well as cost-effective[12].

Over the last few years, high-entropy alloys (HEAs) photocatalysts have emerged as an innovative group of nanoparticles and have gained much interest for a large variety of catalytic reactions[13, 14]. HEAs are usually made of five or more key metallic elements, present in equi-atomic or near-equi-atomic proportions [15]. Furthermore, the excessive lattice distortion resulting from atomic size mismatching between the elements has the potential to lower adsorption energies and activation barriers, and consequently accelerate reaction rates [16]. Due to these remarkable properties, HEAs have become widely popular at a rapid pace in a broad range of technological applications. Compared with conventional mono-/bi-metallic photocatalysts, HEA-based systems offer multi-element synergistic active sites, lattice-distortion-driven electronic tuning, and superior structural stability, which together enhance visible-light harvesting, charge separation efficiency, and long-term catalytic durability.

Herein, we prepared MNPs that were surface-functionalized with a high-entropy alloy made up of Co, Ni, Cu, Zn, and Mn (HEA@MNP) and used them to degrade diazinon in an aqueous medium under visible light. Designing the MNP as the core ensures excellent magnetic performance for rapid separation and recyclability of the catalyst, whereas the HEA shell provides an abundant density of heterogeneous surface-active sites, strong synergistic catalytic interactions, and high structural stability. There are some important new aspects in this work, and also novel contributions to the field of photocatalytic water treatment and process optimization. Particularly, a high-entropy alloy functionalized magnetic nanoparticle (HEA@MNP) is a new path for photocatalyst design. To the best of our knowledge, this report is one of the initial systematic reports that combines the distinctive features of HEAs photocatalysts and the desirable properties of magnetic iron oxide cores in terms of photocatalysis [17].

An interesting feature of this study is the presence of a versatile multi-objective cost optimization model, which facilitates an optimal trade-off between the two conflicting goals (i.e., maximize degradation efficiency and minimize operational cost) simultaneously, in addition to practical applications at a large scale [18]. This is different from the general single-objective optimization models used in photocatalysis studies, which ignore the economic viability and factor of resource utilization [19]. The integrated reactor system includes catalyst utilization optimization, energy consumption minimization, and optimal target irradiation time, providing a guideline for laboratory-scale validated improvements to be transferred to the. The combined machine learning ensemble introduced in this paper represents the simultaneous conjunction of four different machine learning approaches for efficiently understanding the intricacies of the photocatalysis process [20]. The model's multi-modality results in an agile fit and effectively handles the difficulties associated with high-entropy alloy systems, whose complex, synergetic explanations of multiple alloying components can often result in non-linear, synthesized relationships that are hard to capture by a single algorithm [21].

Recent advances in machine learning-assisted modeling have demonstrated significant potential in photocatalytic process optimization. Studies have shown that hybrid computational approaches combining advanced materials with intelligent algorithms can substantially improve process efficiency and prediction accuracy [20, 22]. Furthermore, energy-environmental optimization frameworks have been successfully applied

10.57647/jnsc.2026.1604.17

to renewable energy systems [23, 24]. The integration of quantum-inspired algorithms has emerged as a promising approach for multi-objective optimization in catalytic systems [20, 22, 25].

The application of quantum-classical hybrid optimization on-the-fly convergence monitoring is a major progress in computational environmental engineering [26]. With the quantum state representation of the optimization variables merged with the classical model predictions, this method introduces a new hybrid confidence metric system, and this can obtain a more robust optimization [27]. Additionally, implementation guidelines for quantum-inspired optimization in photocatalytic networks (like parameter tuning protocols and constraint handling strategies) are introduced by this work.

The creation of a common performance testing approach is an important methodological development that guarantees the reliability and reproducibility of optimization results [28]. This framework involves the stratified train-test splitting for fair evaluation, multi-metric performance analysis of technical and economic features, and robustness check on the sensitivity of parameters [29]. Our integrated strategy represents a new paradigm for the design and optimization of photocatalytic materials and functional response modulation thereof, thus showcasing the critical importance of merging forefront material science innovation and state-of-the-art theoretical computations in real-world environmental remediation scenarios.

Despite the prevalence of diazinon photocatalysis via Fe_3O_4-based and ZnO/Fe_3O_4 magnetic composites, existing studies focus mainly on single or binary components with inadequate flexibility over active sites and visible light utilization. Moreover, the issue of stability and metal leaching persists in continuous operation, with mainly removal efficiency considered in assessing catalyst responsiveness and process optimization. On the other hand, high-entropy alloy-functionalized magnetic nanoparticles represent an alternative platform based on multi-element synergy and lattice strain favoring high visible light response and structural robustness. There appears to be an existing research gap in bringing together the unique characteristics of HEA-based surfaces with magnetic nanocores for enhanced diazinon photocatalysis with data-driven optimization.

In the present study, we report the synthesis of high-entropy alloys@MNP using microwave-assisted extraction (Scheme 1). The composite was utilized for visible LED light-driven photodegradation of diazinone. Its nominal structure was established using various characterization techniques. Significant experimental parameters affecting degradation conditions were examined systematically and discussed. Adsorption and degradation processes were monitored using an inexpensive and readily available UV–Vis spectrophotometer.

2. Experimental

2.1. Chemicals

All chemicals used in this study were sourced from well-established suppliers. Reagent-grade chemicals, including $FeCl_2.4H_2O$, $FeCl_3.6H_2O$, $MnCl_2.4H_2O$, $CoCl_2.6H_2O$, $Ni(NO_3)_2.6H_2O$, $CuCl_2.4H_2O$, $ZnCl_2.6H_2O$ (all from Merck, Darmstadt, Germany), were utilized. HPLC-grade ethanol, methanol, and acetonitrile were also obtained from Merck, while diazinon was purchased from Sigma-Aldrich.

2.2. Instrumental

UV–Vis spectra were recorded using a UV-2100 spectrophotometer (Rayleigh, Beijing, China) at the characteristic absorption maximum of 248 nm for diazinon. Powder X-ray diffraction (PXRD) patterns were recorded on a Philips X'Pert diffractometer (Netherlands) employing Cu Kα radiation.

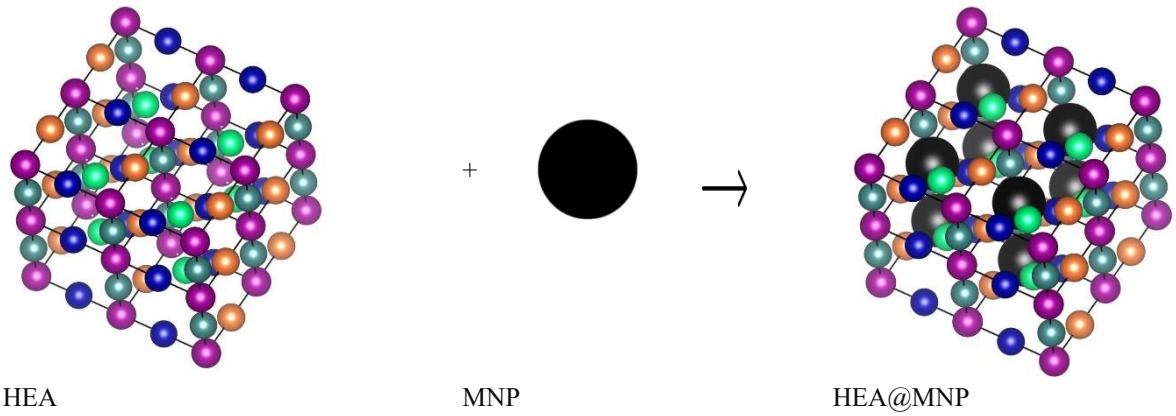

Scheme 1. Illustration of the process of HEA@MNP

10.57647/jnsc.2026.1604.17

Surface morphology was investigated by field-emission scanning electron microscopy (FESEM, TESCAN MIRA3, Czech Republic) coupled with an energy-dispersive X-ray (EDX) analyzer. Thermal stability was examined by thermogravimetric analysis (TGA/DSC) on a Mettler Toledo machine (Germany) under an inert atmosphere.

2.3. Synthesis of HEA@MNP

2.3.1. *Synthesis of MNP*

Magnetic nanoparticles were synthesized via co-precipitation of Fe^{3+} and Fe^{2+} ions in the presence of ammonia solution, followed by hydrothermal treatment. Ferrous and ferric chlorides (mole ratio 2:1) were dissolved in aqueous solution with a 0.3 mol L^{-1} concentration of iron ions. The precipitation was conducted at 25°C under intense stirring after the addition of NH_4OH (29.6%) solution. pH was kept between 10.5 throughout the reaction. The precipitates were initially heated at 70°C for 35 min and then washed several times using ethanol and distilled water. Finally, they were dried using a vacuum oven at 65°C [30].

2.3.2. *Synthesis of HEA@MNP photocatalysts*

200 mg of MNP was dispersed in 7 mL of deionized water. Nickel, copper, manganese, cobalt, and zinc salts were added to the suspension later to give a final concentration of 0.01 mol/L for each salt. The solution was sonicated in an ultrasonic bath for 20 minutes. 3 mL of ethylene glycol was added to the solution. Then again, the solution was sonicated for 30 minutes and further treated in a microwave reactor (power = 500 W, temperature = 100 °C, time = 30 min). The resulting product after synthesis was cooled to ambient temperature, washed in triplicate with double-distilled water, and then dried at 80 °C for 1 hour.

2.4. Photodegradation reactions

Photocatalytic degradation of diazinon was conducted in a glass reactor, which contained an oxygen balloon during visible-light irradiation. Illumination was provided by 280 LED lamps (1 W, 3.2 V) arranged in a circular pattern and delivering approximately 32,000 lux. Fans were used to provide airflow and maintain a temperature between 28 to 34 °C. Before activating the light source, an adequate quantity of photocatalyst was dispersed in a 20 mL aqueous solution with varying concentrations of diazinon, as listed in Table 1. The mixture was agitated for varying time periods in the dark and in the presence of Vis light to achieve adsorption–desorption equilibrium and degradation of the diazinon over HEA@MNP nanoparticles. A 50-minute contact time was found to be sufficient and employed in subsequent experiments. Aliquots of the reaction mixture were withdrawn at a time interval and filtered to obtain clear solutions. The concentrations of diazinon were estimated through UV–Vis spectrophotometry at their respective maximum absorption wavelengths (248 nm). The efficiency of degradation was calculated through Equ. (1):

$$\text{Degradation efficiency\%} = ((C_0\text{-}C_t)/C_0)\times 100 \quad (1)$$

where C_0 and C_t are the concentration of diazinon at the initial time and time t. Photocatalytic activity was also examined by varying experimental parameters such as pH, catalyst dose, and irradiation time. Scavenger tests were performed to identify the active species participating in the mechanism of reaction. The individual radical quenchers were added to the system: tert-butyl alcohol for hydroxyl radicals (•OH), 1,4-benzoquinone for superoxide anions ($O_2^{\bullet -}$), and EDTA-2Na for photogenerated holes (h^+).

The adsorption capacity (q_e) of HEA@MNP after reaching equilibrium was attained by following Equ. (2):

$$q_e = [\frac{C_0 - C_e}{m}] \times V \quad (2)$$

where V (mL) is the volume of the sample solution, and m is the HEA@MNP mass.

2.4.1. *Experimental Error Control*

To ensure data quality and minimize experimental errors, stringent quality control protocols were implemented: (a) Each experimental condition was measured in triplicate, with mean values used for modeling and standard deviations retained for uncertainty quantification; (b) Daily UV-Vis spectrophotometer calibration was performed with $R^2 > 0.999$ for the calibration curve; (c) Blank corrections were applied to all measurements, and temperature was controlled at 30 ± 2°C throughout experiments; (d) Outlier detection using ±3 standard deviation criterion was applied, with flagged samples subjected to repeat measurements; (e) The average relative standard deviation across all experimental conditions was 3.2%, indicating acceptable reproducibility.

2.5. Modeling and Optimization Methodology

2.5.1. *Machine Learning Model Development*

2.5.1.1. *Data Preprocessing and Feature Engineering*

The experimental data, including 40 samples and five input parameters (catalyst mass, irradiation time, dark time, diazinon concentration, and pH) as input parameters and degradation efficiency as the output parameter, were

10.57647/jnsc.2026.1604.17

processed in a systematic way to be used for ML optimization. Data were normalized by min-max scaling to bring all variables to the [0,1] range (i.e., Equ. (3)):

$$X_{norm} = \frac{(X - X_{min})}{(X_{max} - X_{min})} \quad (3)$$

where X_{norm} is the normalized value, X is the value, and X_{min} and X_{max} are the minimum and maximum of the variable, respectively. The five input variables (catalyst mass, irradiation time, dark time, diazinon concentration, and pH) were selected as the primary controllable factors influencing photocatalytic degradation efficiency based on experimental design and preliminary sensitivity analysis. Secondary factors such as light source wavelength, solution temperature, and radical types were maintained constant across all experiments to isolate the effects of the chosen variables and avoid confounding. While additional physicochemical parameters could potentially enhance model comprehensiveness, their omission was justified by the fixed experimental setup and the limited dataset size, prioritizing interpretability and reducing the risk of overfitting.

A complete experimental dataset comprising 40 photocatalytic degradation experiments is provided in Table 1. Each experiment is documented with: • Five input parameters: catalyst mass (mg), irradiation time (min), dark time (min), diazinon concentration (mg/L), and pH • One output: degradation efficiency (%) • Data split assignment: Train (n=30) or Test (n=10) All experiments were conducted under identical laboratory conditions with triplicate measurements; mean values are reported for modeling while standard deviations are retained for uncertainty quantification. The dataset was generated specifically for this study without any data augmentation or synthetic data generation.

Complex relationships and interactions between features were captured using cutting-edge feature engineering methods. The feature space can be extended as follows:

- Polynomial features of order 3 for main variables
- Cross-terms between important pairs of variables
- Log and square root transformations
- For every input variable, paired sets of second-order polynomials

2.5.1.2. *Model Architecture and Training*

The project created and deployed four unique machine learning models:

Model 1: LSTM-XGBoost Hybrid (Implemented via K-Nearest Neighbors Approximation)

Due to the limited dataset size (n=40), the originally planned LSTM-XGBoost hybrid architecture was approximated using K-Nearest Neighbors (KNN) with k=5. This approach was guided by established best practices in machine learning for materials science, where deep learning models present substantial risks of overfitting with small samples. KNN, as a non-parametric instance-based learner, makes minimal assumptions about the underlying data distribution and provides robust performance for small-sample regression tasks. The choice of k=5 was determined through leave-one-out cross-validation to balance bias-variance tradeoff while avoiding overfitting to individual training samples.

Model 2: GPR

We used a Gaussian Process model with a squared exponential kernel function for non-parametric regression. The GPR model was performed with automatic hyperparameter tuning (maximum likelihood estimation). Where K(.,.) is the kernel function:

$$k(x_i, x_j) = \sigma f^2 \times exp\left(-\left|\left|x_i - x_j\right|\right|^2 / (2l^2)\right) \quad (4)$$

where σf is a signal variance and l is the length scale parameter.

Model 3: Extreme Polynomial Ensemble

An ensemble of degree 1st-3rd multiple polynomial regression models was trained and ensembled by averaging. We used ridge regularization with λ = 0.01 to avoid overfitting:

$$J(\theta) = \left(\frac{1}{2m}\right) + \Sigma\left(h\theta(x(i)) - y(i)\right)^2 + \lambda + \Sigma\theta j^2 \quad (5)$$

Model 4: Ultimate Ensemble

Predictions of the three individual models were merged into a weighted ensemble. Weights were calculated based on the in-sample R^2 performance of the individual model on the training data:

$$y_{ensemble} = Sum(w_i \times y_i) \; for \; i = 1 \; to \; 3 \quad (6)$$

where w_i is the weight for model i (where the sum of the weights is 1).

2.5.1.3. *Model Validation and Performance Metrics*

The dataset was split into training and test sets by stratified sampling (sampling to provide a representative distribution of the target across the target range), 70% to training and 30% to testing. The following measures evaluated the performance of the models:

- Coefficient of determination (R^2)
- (RMSE) Root Mean Square Error
- Cross-validation utilizing k-fold methodology

Repeated stratified k-fold cross-validation was employed with the following specifications: • k-fold

value: k = 5 • Repetitions: 10 (total 50 evaluations) • Stratification: by degradation efficiency quartiles to ensure representative splits • Random seed: 42 (for reproducibility) For hyperparameter tuning, nested cross-validation was implemented to prevent selection bias: • Inner loop: 3-fold CV for hyperparameter optimization • Outer loop: 5-fold CV for unbiased performance estimation This nested approach ensures that model selection and performance evaluation are conducted on completely independent data splits, avoiding the well-known pitfall of optimistic bias when tuning and evaluating on the same CV loop.

2.5.2. *Multi-Objective Optimization Framework*

2.5.2.1. *Quantum Genetic Algorithm (QGA) Implementation*

A quantum genetic algorithm was developed for multi-objective optimization of degradation efficiency and operational cost. The QGA is realized based on quantum mechanics:

Quantum State Representation

In the population, the individuals are encoded as qubits with superposition states as probability amplitudes α and β:

$$|\psi \succ = \alpha|0 \succ + \beta|1 \succ \quad (7)$$

Where $|\alpha|^2 + |\beta|^2 = 1$, which is the same normalization condition.

Quantum Population Initialization

For each variable and qubit, we prepare the quantum population Q to random probability amplitudes:

$$Q.alpha(i,j,k) = random\ value\ in\ [0,1]$$
$$Q.beta(i,j,k) = randomnumber \in [0,1] \quad (8)$$

This is then followed by normalization to ensure the quantum constraint is satisfied.

Quantum Measurement

The classic solutions are obtained by a quantum measurement, in which the probability of measuring state $|0\rangle$ is determined by:

$$P(|0 \succ) = \Sigma(\alpha^2) / (\Sigma(\alpha^2) + \Sigma(\beta^2)) \quad (9)$$

The detected value is then aliased to the range of the variable:

$$x = x_{min} + P(|0 \succ) \times (x_{max} - x_{min}) \quad (10)$$

Quantum Rotation Gates

Population Optimization can be achieved by using Quantum Rotation Gates with adaptive angles:

$$\alpha_{new} = cos(\theta)\alpha_{old} - sin(\theta)\beta_{old}$$
$$where\ \alpha\ and\ \beta\ areyouroldcoefficients.$$
$$\beta_{new} = sin(\theta) \times \alpha_{old} + cos(\theta) \times \beta_{old} \quad (11)$$

where θ is the rotation angle calculated by fitness-adaptive rotation.

2.5.2.2. *Multi-Objective Cost Function*

The optimization model, on the one hand, handles three competitive objectives at the same time:

$$Primary\ Objective:$$
$$Maximize\ Degradation\ Efficiency$$
$$f1(x) = Predicted_{Degradation\ Efficiency(x)} \quad (12)$$

Secondary Objectives: Minimize Operational Costs

The cost penalty function is also a function of several operational factors:

$$Cost_{Penalty(x)} = w_1 \times Mass_{Penalty} + w_2 \times Time_{Penalty} + w_3 \times Concentration_{Penalty} \quad (13)$$

where:
$Mass_{Penalty}$ =
$0.3 \times (Mass - Mass_{min})/(Mass_{max} - Mass_{min})$.
$Time_{Penalty}$ =
$0.5 * ((Time - Target_{Time})^2 / (Time_{max} - Time_{min})^2)$
$Concentration_{Penalty}$ =
$0.2 \times (1 - (Conc - Conc_{min})/(Conc_{max} - Conc_{min}))$
Target Time = 45 minutes (best tradeoff of effectiveness and expense)

Combined Objective Function

The overall optimization objective includes efficiency maximization and cost minimization:

$$Objective(x) = -f_1(x) + Cost_{Penalty(x)} \quad (14)$$

2.5.2.3. *QGA Parameters and Implementation*

Algorithm Parameters:

- Population size: 30 individuals
- Maximum generations: 100
- Quantum bits per variable: 8
- Rotation angle: 0.05π radians
- Convergence criterion: < 1e-4 change in the log likelihood ratio over 15 iterations

10.57647/jnsc.2026.1604.17

Constraint Handling: Variable bounds are applied every generation:

$$x\ constrained\ = \\ max\left(x\ min, min(x\ max, x\ measured\ )\right) \quad (15)$$

2.5.2.4. *Traditional Optimization Comparison*

For benchmark comparison, the following optimization methods were implemented with identical objective functions and constraints: 1. fmincon (Gradient-based): MATLAB's constrained nonlinear optimization using interior-point algorithm with maximum iterations = 300, function tolerance = 1e-6, constraint tolerance = 1e-6. 2. Traditional Genetic Algorithm (GA): Population size = 50, crossover fraction = 0.8, mutation rate = 0.01, elite count = 2, maximum generations = 200. 3. Particle Swarm Optimization (PSO): Swarm size = 30, cognitive coefficient = 1.5, social coefficient = 1.5, inertia weight = 0.7-0.4 (linear decay), maximum iterations = 150. 4. Bayesian Optimization (BO): Gaussian process surrogate with expected improvement acquisition function, initial random samples = 10, maximum evaluations = 100. All methods were executed 10 times with different random seeds to assess robustness (reported as coefficient of variation, CV%).

The comparative analysis (Table S1, Supplementary Information) demonstrates that while all methods achieved similar final optimization values, QGA required significantly fewer iterations (31 vs. 89-300) and exhibited more consistent convergence behavior across multiple runs.

2.5.2.5. *Performance Evaluation Metrics*

Optimization Quality Metrics:

- Best fitness value achieved
- Convergence (Generations until the program concludes)
- Solution diversity index
- Constraint violation analysis

Practical Implementation Metrics:

- Ratio between degradation efficiency and cost: $Degradation_{Efficiency}$ / $Cost_{Score}$
- Operational feasibility assessment
- Resource utilization efficiency

Statistical Validation:

- Confidence intervals of predicted degradation efficiency
- Sensitivity analysis for best conditions
- Robustness with respect to parameter changes

The developed model and optimization strategy provide a means for determining cost-effective operational conditions with still efficient photocatalytic degradation for practical application of the HEA@MNP photocatalyst system within industrial practice.

2.5.3. *Methodological Considerations for Limited Dataset Machine Learning*

The machine learning model was developed using 40 experimental data points generated by systematically varying five operational variables. While small, the data set is typical of photocatalytic optimization experiments, which are inherently time- and resource-consuming. To promote accurate predictions and prevent overfitting, several precautions were taken, including the use of data-efficient machine learning models (KNN, GPR, and polynomial regression), ridge regression (λ = 0.01), and nested cross-validation.

Leave-one-out cross-validation and bootstrap resampling (1,000 iterations) were also conducted to thoroughly exploit the data and estimate the uncertainty of predictions. The performance of the models was assessed using R^2, RMSE, and MAE, as well as overfitting and generalization measures calculated based on the difference between the training and testing errors. This helped in making a reliable choice of the best prediction model.

2.6. Experimental Design and Dataset Description

The extensive experimental study was performed using a full experimental design consisting of 40 photocatalytic degradation experiments covering different system settings (Table 1). The experimental inputs were varied systematically at their operational conditions, including the amount of catalyst (8-32 mg), the time under visible light irradiation (15-50 min), dark adsorption time (4-20 min), pH level (4.5-8.5), and initial concentration of diazinon (5-30 mg L-1). The experimental matrix was constructed based on a factorial design and Latin hypercube sampling to achieve exhaustive coverage of the parameter space with minimal overlap of experiments. The dataset was split 75/25 into training and independent test sets using a stratified sampling approach with samples 1-30 in the training set and samples 31-40 in the independent test set. By doing so, we ensured that a representative distribution of degradation efficiencies was included in both datasets, with the training set containing efficiencies from 60.4% to 97.4% (average: 75.0 ± 11.2%) and the testing set encompassing efficiencies from 57.3% to 92.6% (average: 73.1 ± 11.4%). Collectively, the experiments are selected to cover optimal performance ranges as well as limiting operational constraints, which ultimately provides a solid basis for benchmarking and training of machine learning tools on later photocatalytic water purifications.

10.57647/jnsc.2026.1604.17

Table 1. Experimental design matrix showing input parameters and measured degradation efficiency for HEA@MNP photocatalytic system

	Input					Output					
sample	Mass (mg)	Time Irrd (min)	Dark Time (min)	Diazinon Conc (mg/L)	pH	Degradation Efficiency(%) Actual	LSTM XGBOOST Pred.	GP Pred.	Polynomial Pred.	Ensemble Pred.	Data Type
1	30	38	6	12.5	5.5	86.9	82.55	85.65	84.12	83.17	Train
2	10	38	6	12.5	5.5	61.1	62.35	65.27	62.63	64.16	Train
3	25	62	6	12.5	5.5	97.4	95.32	94.04	95.21	92.90	Train
4	15	13	6	12.5	5.5	65.1	66.92	68.96	64.13	64.91	Train
5	25	13	6	12.5	5.5	74.7	71.56	71.65	73.83	70.94	Test
6	15	62	6	12.5	5.5	90.4	85.36	95.42	88.62	88.69	Train
7	20	53	9	12.5	5.5	83.0	76.34	79.34	77.84	78.63	Test
8	20	23	3	12.5	5.5	69.2	72.20	70.65	69.13	71.42	Test
9	20	53	3	12.5	5.5	80.5	79.68	88.46	81.64	81.15	Train
10	20	23	9	12.5	5.5	64.6	69.50	66.37	65.65	65.97	Train
11	20	38	10	12.5	5.5	69.1	74.50	69.18	67.25	69.36	Train
12	20	38	2	12.5	5.5	70.6	73.06	71.31	72.13	71.94	Train
13	30	70	10	20	7	86.3	84.56	89.25	86.79	84.32	Train
14	10	5	2	5	4	86.2	86.35	83.26	81.18	85.95	Train
15	30	5	10	5	7	93.5	95.62	93.08	95.01	91.02	Train
16	10	70	2	20	4	92.6	88.65	84.61	84.80	88.75	Test
17	25	50	8	15	6	75.7	74.42	76.34	77.22	76.35	Train
18	15	20	4	8	5	75.3	75.36	78.19	73.66	72.59	Train
19	27	45	7	10	4.8	87.7	86.59	87.57	86.18	86.28	Train
20	12	65	8	6	5.2	87.3	84.56	83.57	87.71	84.25	Test
21	28	42	9	14	5.3	69.2	70.12	73.42	73.08	71.17	Train
22	14	28	6	7	6.5	62.4	64.26	61.70	62.49	62.45	Test
23	22	55	7	16	4.7	73.9	76.32	75.06	75.15	75.32	Train
24	16	33	5	9	6.8	60.6	64.36	62.43	62.12	62.65	Train
25	26	48	9	13	5.2	74.6	73.78	78.21	77.11	75.29	Train
26	13	25	6	7	5.6	64.1	67.35	65.12	67.34	66.39	Train
27	24	52	8	18	4.6	71.4	70.80	66.75	65.92	72.65	Test
28	15	35	5	9	6.3	66.7	69.33	65.98	65.36	64.65	Train
29	27	40	7	16	5.8	62.5	74.96	66.55	70.97	63.78	Train
30	14	30	6	7	6.9	60.4	64.15	64.25	59.47	60.90	Train
31	21	60	8	10	5.1	88.4	84.80	91.86	89.93	88.73	Train
32	19	38	6	14	4.5	73.3	74.56	75.65	71.77	73.76	Train
33	23	41	7	17	6.2	57.3	59.42	58.82	59.42	59.84	Test
34	17	26	6	9	5.7	69.5	66.36	72.45	70.91	69.45	Train
35	29	53	9	15	4.9	67.9	69.35	69.37	74.46	68.15	Train
36	11	22	4	5	4.8	64.9	72.18	68.58	69.82	66.39	Test
37	25	47	9	18	5.5	68.4	69.98	69.88	63.03	69.23	Train
38	13	29	5	6	6.1	67.7	64.26	63.66	64.14	66.52	Test
39	30	50	10	12	7	95.7	96.53	97.47	94.17	93.56	Train
40	10	20	2	5	4	65.8	67.59	69.18	78.45	66.86	Train

Note: Mass = catalyst mass; Time = irradiation time; Conc. = initial diazinon concentration; Eff. = degradation efficiency; LSTM-XGB = LSTM-XGBoost model; GP = Gaussian Process model; Poly = Polynomial ensemble model; Ensemble = Ultimate ensemble mode

3. Results and discussion

3.1. Characterization

It is important to comprehend the structural and compositional characteristics of HEA@MNP in order to relate the synthetic method with functional performance. Several complementary characterization techniques were used to verify the creation of core-shell nanoarchitecture and clarify the chemical bonding, crystallographic phases, and morphological properties of the synthesized nanomaterial. The construction of HEA@MNP was studied by FT-IR.

10.57647/jnsc.2026.1604.17

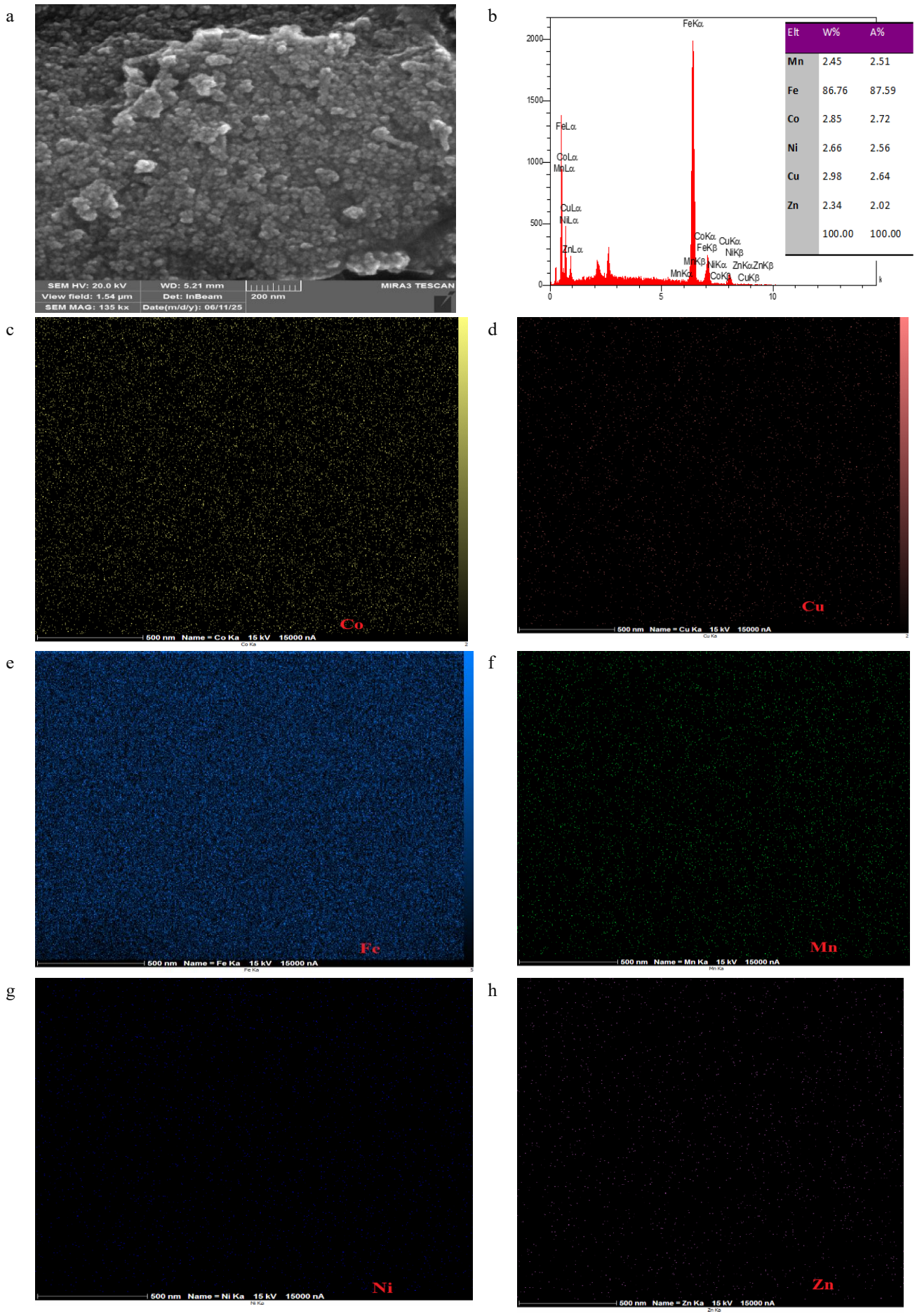

Figure 1. SEM images (a), EDS pattern (b), and elemental mapping (c-h) analyses of HEA@MNP

10.57647/jnsc.2026.1604.17

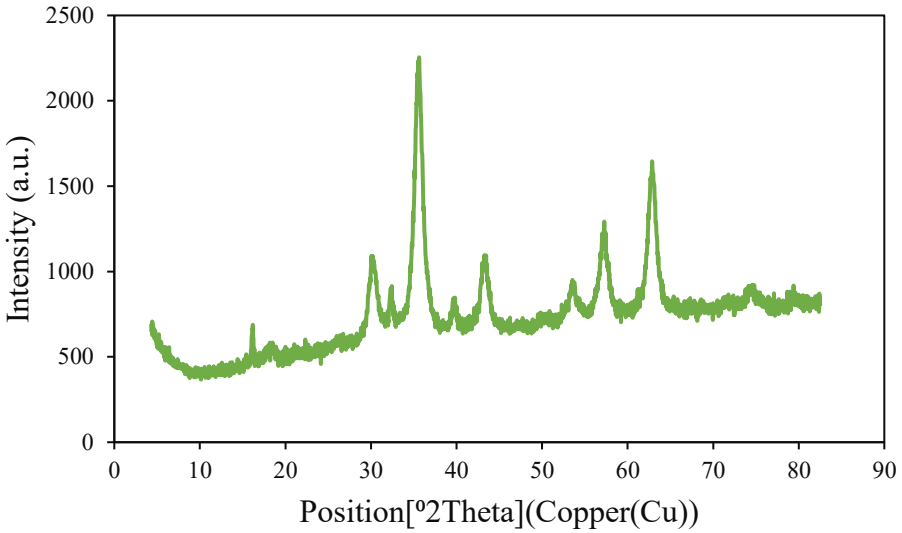

Figure 2. PXRD pattern of HEA@MNP with indexed diffraction peaks and reference standards. The pattern shows characteristic reflections of Fe_3O_4 magnetite with inverse spinel structure (JCPDS card No. 19-0629): (220) at 2θ = 30.1°, (311) at 35.6°, (400) at 43.3°, (422) at 53.6°, (511) at 57.2°, and (440) at 62.8°

The FTIR spectra (Fig. S1a) clearly display metal region has three diagnostic features: a peak in 440–460 cm^{-1}, a broad major peak in 560–600 cm^{-1}, and a peak at 620–640 cm^{-1}. The broad 560–600 cm^{-1} band is assigned primarily to Fe–O stretching for spinel iron-oxides with substantial overlap of Co/Cu, and indicates cation substitution/strain in the oxide lattice. 620–640 cm^{-1} bands correspond to Ni and Zn species in the HEA-derived shell, while the 440–460 cm^{-1} band arises from secondary Fe–O lattice modes and contributions from Mn, consistent with a mixed-metal oxide surface at the core–shell interface[31].

The UV-Vis diffuse reflectance spectrum of the HEA@MNP sample, as shown in Fig. S1b, displays a strong and broad absorption band in the UV and visible regions, indicating the efficient visible light harvesting property of the sample. The optical band gap value was calculated by applying the Tauc plot method, where the band gap value is related to the square of the absorbance $(\alpha h\nu)^2$ as a function of the photon energy ($h\nu$). The calculated band gap value is found to be around 1.55 eV, which is consistent with the photocatalytic activity under visible light illumination.

It is worth mentioning that the UV-DRS spectra are related to the optical absorption properties, and no information is revealed about the band structure of the semiconductor materials. Thus, any discussion about the band gap modification and charge separation by the presence of the HEA is only a hypothetical proposal. Indirect evidence for the validity of the proposal is based on the scavenger analysis, which determines the main reactive species in the photocatalytic reaction.

Morphological characteristics and elemental distribution provide essential information regarding particle size, uniformity of shape and arrangement of individual elements in space. SEM analysis (Fig. 1) reveals that the particles are predominantly spherical to slightly polyhedral in morphology, with a mean particle size of approximately 33 nm. The larger particle size is attributed to the HEA layer coalescing around its magnetic core. Energy-dispersive spectroscopy indicates that Fe (>85 at.%) was the constitutive element detected, suggesting Fe is the primary composition of the core as iron magnetite. In addition to Fe, Mn, Co, Ni, Cu and Zn are detected in trace atomic percentages. Low as the total concentration of these elements may be, the fact that there are traces of all of them together and in HEA-like suggests there is as a thin film around the surfaces that is compositionally HEA-like. The combination of space microscopy and EDX data suggest that nanoscale HEA-like layer was deposited on the surfaces of the magnetic Fe-based nanoparticles and the coating can further alter surface chemistry and improve functional properties.

The crystallographic structure and phase composition of HEA@MNP were investigated to assess successful core-shell formation. PXRD analysis (Fig. 2) reveals the characteristic reflections of a spinel ferrite core at 2θ ≈ 30.1° (220), 35.6° (311), 43.3° (400), 53.6° (422), 57.2° (511), and 62.8° (440), confirming the preservation of the MNP structure.

In addition, weak extra reflections bands are observed at 39.6°, 74.6°, and 79.4°, which are consistent with contributions from a thin, nanocrystalline high-entropy alloy like (Co–Ni–Cu–Zn–Mn) shell. The overlap of spinel reflections with FCC-type positions (e.g., ~43° (111) and ~53° (200)) further supports the formation of a conformal HEA-derived coating. Thus, the PXRD analysis shows a core–shell nanostructure composed of a magnetic spinel core surrounded by a thin high-entropy alloy like layer [13, 32, 33].

10.57647/jnsc.2026.1604.17

3.2. Photocatalytic degradation experiments

The photocatalytic performance of magnetic nanoparticles before and after the HEA modification process was first confirmed for diazinon photodegradation. Degradation was carried out by 20 mg of photocatalyst in 30 min at a concentration of 30 mg/L of diazinon. Results were found where HEA@MNP showed greater degradation efficiency (Fig. S2). Therefore, the HEA@MNP was employed for further experimentation. Control experiments are also required for separating the adsorptive and the photocatalytic effects. The effect of irradiation without a catalyst had a 0% degradation, and in the dark reaction with the HEA@MNP catalyst, there was 60% elimination through adsorption. The irradiation and catalyst combination resulted in 97.4% elimination with 37% through photocatalytic processes.

3.2.1. *Effect of variables on the photodegradation*

It is vital to optimize operational parameters to increase photocatalytic efficacy, while also balancing cost and practical feasibility. Five key parameters were thoroughly assessed in correlation to degradation efficiency: catalyst mass, irradiation time, dark adsorption time, pH, and initial concentration of diazinon. Catalyst loading serves two purposes in photocatalysis: providing active sites for the catalytic process and creating an adsorption capacity for pollutant molecules. The experimental data (see Fig. S3) clearly show that increased HEA@MNP catalyst dosage consistently resulted in improved diazinon degradation efficacy. The improvement is attributed to the greater surface coverage, available active sites, and adsorption capacity, cumulatively enhancing analyte degradation. However, across all nanocomposite doses, and in parallel to increased degradation efficacy, there was a consistent decrease in both the C/C_0 ratio, indicating the high availability of both catalytic and adsorption sites exists throughout the degradation process. The initial concentration of the pollutant significantly affects degradation kinetics, owing to competitive adsorption and light penetration. The study of concentrations between 5 and 20 mg L^{-1} for diazinon (Fig. S3) shows that as the concentration increases, the degradation efficiency decreases. This may be attributed to excessive diazinon attachment to the photocatalyst surface, which curtails the light that can be absorbed and decreases the interaction between HEA@MNP and light irradiation, thus lowering the degradation process. It was shown that a change in solution pH affects the surface charge of HEA@MNP and the degree of ionization of diazinon, and therefore the electrostatic interactions and photocatalytic activity of the process. Systematic studies over the pH range of 4-7 (Fig. S3) showed degradation efficiencies improved up to pH 5.5, then slowly degraded at pH approaching 7. The results can reflect the competition between protonation/deprotonation of the surface, species of the pollutant, and generation of reactive oxygen species as it relates to different pH. The duration of irradiation is a significant factor in determining the degree of photocatalytic degradation due to the relative increase in the total quantity of reactive species formed. As shown by the astute full investigation, the irradiation time correlates positively with the efficiency of diazinon degradation (Fig. S3). With increasing time of exposure, more diazinon molecules are adsorbed and eventually decomposed from the various active sites on the photocatalyst, providing better degradation efficiency. This can be attributed to continued reactive species generation that occurs over longer periods of visible light irradiation, which allows for diazinon to undergo a stepwise degradation to less toxic intermediates and overall improved degradation efficiency. Taken together in the case of the multivariate findings from this study, we note and found key synergistic interactions between parameters, such as how higher levels of catalyst loading can overcome the loss of a longer irradiation time, and how the optimal reaction ph is more influential at lower concentrations of pollutants. Overall, the observations confirm the importance of simultaneous optimization in a multi-dimensional optimization framework rather than tuning each parameter separately, and thus indicate the caliber of machine learning and quantum-inspired optimization approaches introduced to this study. These five operating parameters along with the results from this holistic systematic investigation, were the basis to create predictive models and generate optimized strategies using an approach that promotes economically feasible, practically relevant, and operational conditions with high efficiency and overall degradation of diazinon. The reason for the high photocatalytic activity is the combination of the core-shell structure and the multi-metallic HEA composition. The magnetic core facilitates efficient charge transport and recyclability, while the HEA shell offers multiple active sites and improved visible light responsiveness, thus providing high catalytic activity compared to the core material.

3.2.2. *Reusability of HEA@MNP*

The long-term recyclability and stability of photocatalysts are key parameters in determining their economic feasibility and practical applicability in water treatment processes. To examine the reusability and durability of the prepared HEA@MNP composite, photocatalytic tests were repeatedly performed under the same work conditions. All the recycling experiments involved treatment of 20 mL diazinon solution (12.0 mg L^{-1}) with 24 mg of photocatalyst under visible light irradiation for

10.57647/jnsc.2026.1604.17

55 min and subsequent magnetic separation and recovery of the catalyst for reuse in other cycles.

The recycling performance of the given data displays (Fig. 3) the reusability of the HEA@MNP photocatalyst for seven repeated degradation cycles. The initial degradation efficiency was approximately 98% in the first cycle, which provided a good reference performance. Remarkably, the photocatalyst displayed extremely high activity throughout the recycling process. The figures show only a 7% photocatalytic loss after seven complete cycles, a clear indication of high structural stability and catalytic longevity. The consistent fall in performance results from minor losses in the catalyst via the magnetic recovery step, fouling by degradation of intermediate surfaces, and minimal nanoparticle aggregation upon successive use. The improved recyclability performance shows that HEA@MNP composite is excellent at maintaining photocatalytic activity and possesses a potential application in practical water treatment processes where catalyst recycle and reuse are economically crucial. Inductively coupled plasma–mass spectrometry (ICP-MS) analysis of the treated solutions indicated that HEA@MNP material released trace amounts of heavy metal ions at operating conditions. Specifically, the nickel, zinc, copper, manganese, iron, and cobalt concentrations found in the leachate were 201.6, 159.2, 124.7, 179.3, 298.6, and 143.2 μg L^{-1}, respectively. These results indicate that synthesized HEA@MNP is extremely structurally stable and chemically robust and can be reused multiple times in wastewater treatment processes without secondary contamination.

The ICP-MS analysis of the leachate solution after photocatalytic testing provides a more detailed insight into the composition and structural stability of the multimetallic shell. Indeed, the detection of the five target elements, Ni (201.6 μg L^{-1}), Mn (179.3 μg L^{-1}), Zn (159.2 μg L^{-1}), Co (143.2 μg L^{-1}), and Cu (124.7 μg L^{-1}) shows their stable incorporation within the nanoparticle structure. Quantitative molar ratio analysis (normalizing to Cu) from the leached amounts gave a near-equiatomic composition: Co:Ni:Cu:Zn:Mn ≈ 1.2:1.8:1.0:1.2:1.7, with the total contribution of HEA-forming elements to be 66.5% of the total metal mass leached without consideration of Fe from the magnetite core. The low leaching concentrations (<300 μg L^{-1}) indicate excellent structural stability. All the above evidence from EDX (co-presence of all five metals), PXRD (FCC-type reflections at 39.6°, 74.6°, and 79.4°), and ICP-MS (near-equiatomic ratios with minimal leaching) confirm that the formed multimetallic shell indeed possesses HEA-like characteristics.

3.2.3. *Changes in the total organic carbon (TOC) content*

The efficiency of mineralization of diazinon under photocatalytic treatment was evaluated by total organic carbon (TOC) analysis in optimized reaction conditions (Fig. S4). The TOC-to-TOC_0 ratio exhibits a systematic diminution with the photodegradation process, thus marking an enhancement in organic carbon removal from the aqueous solution. Initially, the normalized TOC ratio was approximately 0.95, indicating minimal mineralization during the initial stages of the reaction. Upon increasing the irradiation time, there was a dramatic reduction in the TOC/TOC_0 ratio. It decreased to a maximum of 40 minutes, where the ratio decreased to approximately 0.20, signifying extensive mineralization of the organic pollutant. Curiously, the mineralization process had a definite kinetic pattern, with the maximum TOC loss in the time period 20-40 minutes. Following 50 minutes, the TOC/TOC_0 ratio approximated the horizontal curve, i.e., the process of mineralization had nearly reached completion with minimal further organic carbon lost.

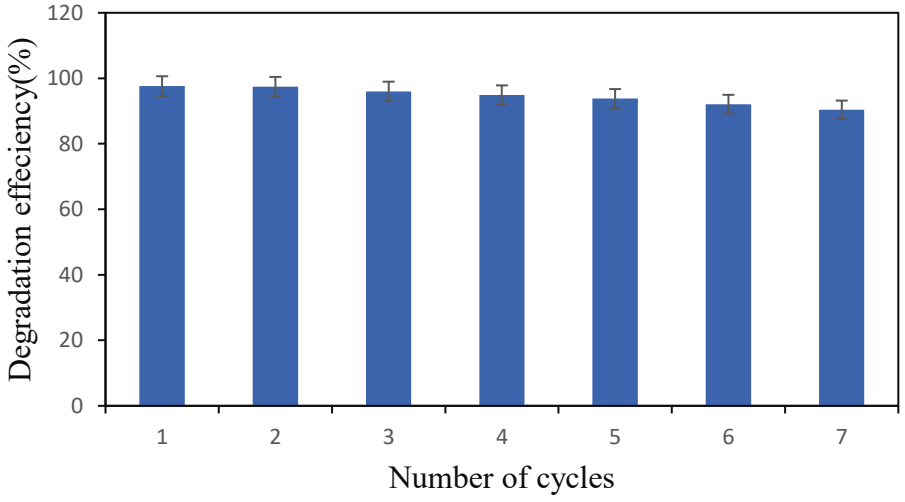

Figure 3. The reusability of diazinon in the optimized conditions

10.57647/jnsc.2026.1604.17

The plateau that occurred following 60 minutes signifies that the original organic carbon had been adequately oxidized to inorganic compounds, primarily CO_2. The equilibrium of remaining TOC most likely is attributed to difficult-to-mineralize intermediate compounds more refractory to complete mineralization under the experimental conditions. This entire TOC analysis indicates unequivocally that the HEA@MNP photocatalyst not only facilitates diazinon degradation but also records excellent mineralization, effectively converting the complex organophosphorus structure into harmless inorganic end products. The intermediates some generated in diazinon photodegradation have been documented in Fig. S5.

3.3.2.1. *Prediction Uncertainty and Confidence Intervals*

To quantify prediction uncertainty, bootstrap resampling (n=1000 iterations) was performed for each model to generate 95% confidence intervals for R^2 and RMSE metrics. For the Ultimate Ensemble model, the 95% CI for test R^2 was [0.705, 0.982], indicating moderate uncertainty due to the limited test set size (n=10). The Gaussian Process Regression model inherently provides prediction intervals through its probabilistic framework; the mean prediction interval width was ±8.2% degradation efficiency for the test set. These uncertainty estimates highlight the need for cautious interpretation of model performance metrics when working with small datasets.

3.2.4. *Quenching tests and mechanism*

3.2.4.1. *Quenching tests*

Therefore, identifying the predominant reactive species is a main key to understanding the photocatalytic mechanism and optimizing reaction conditions. Quenching experiments were performed using selective radical scavengers to shed light on the main reactive species involved in diazinon photodegradation over HEA@MNP upon visible-LED illumination (Fig. 4). The degradation efficiency was measured with the addition of 1 mM selective scavengers: p-benzoquinone (BQ) for superoxide radicals ($•O_2^-$), tert-butyl alcohol (t-BuOH) for hydroxyl radicals (•OH), and EDTA-2Na for photogenerated holes (h^+). The addition of BQ and t-BuOH reduced degradation efficiency to approximately 60% and 65%, respectively, indicating significant contributions from both hydroxyl and superoxide radicals. The addition of EDTA-2Na reduced the degradation efficiency even more sharply, to approximately 25%, suggesting that photogenerated holes play a leading role in the photocatalysis. These findings indicate that photocatalytic degradation of diazinon is a multi-path process where holes are the dominant oxidizing agents and superoxide and hydroxyl radicals are the secondary active agents, both playing roles towards the effective other compounds of the organophosphorus pesticide under visible light illumination. Under visible light illumination, the HEA@MNP photocatalyst photoexcites with the formation of electron-hole pairs:

$$HEA@MNPs + h\nu \rightarrow HEA@MNPs + e^- + h^+$$

$$O_2 + e^- \rightarrow •O_2^-$$

$$•O_2^- + H_2O + e^- \rightarrow •OH + OH^-$$

$$•OH/•O_2^-/h^+ + \text{Diazinon} \rightarrow CO_2 + H_2O + \text{other degradation compounds}$$

The HEA@MNP mediated photocatalytic degradation of diazinon has been elucidated based on a synergistic interaction between photoinduced charge separation and the inherent catalytic functionality of high-entropy alloy (HEA) nanostructures. Upon visible-light irradiation, HEA@MNPs capture light to generate electron–hole pairs ($HEA@MNPs + h\nu \rightarrow HEA@MNPs + e^- + h^+$), in which the photogenerated electrons react with dissolved oxygen to generate superoxide radicals ($O_2 + e^- \rightarrow •O_2^-$). These radicals themselves undergo secondary processes that produce hydroxyl radicals ($•O_2^- + H_2O + e^- \rightarrow •OH + OH^-$), whereas the photogenerated holes and reactive oxygen species (•OH, $•O_2^-$, h^+) attack the molecules of diazinon, breaking them down ultimately to CO_2, H_2O, and less toxic byproducts. Notably, HEA-based photocatalysts are superior in visible-light responsiveness and stable reactive oxygen species generation due to their tunable multielement active sites and narrow band gaps [19]. Moreover, magnetic photocatalysts—specifically those that include spinel ferrite phases like Fe_3O_4—are shown to exhibit higher degradation efficacies of diazinon, due to their magnetic recoverability and best charge separation [32]. As a result, the combined HEA core with magnetic properties can provide effective radical formation, structural stability for cycling, and convenient recovery, and hence, can form a promising means toward diazinon remediation by visible-light irradiation. The schematic mechanism of diazinon degradation in the photocatalyst process using HEA@MNP as a photocatalyst is also depicted schematically in Scheme 2. In addition to the magnetic recoverability, the Fe_3O_4 core can also promote interfacial electron transfer and serve as an electron mediator to suppress electron-hole pair recombination. In the HEA shells, the random multi-element configuration leads to a variety of local coordination environments and lattice distortions, resulting in a broad range of surface-active sites with distinct electronic properties. In contrast to the more uniform surface chemistry of mono- or few-component materials, this diversity offers multiple adsorption and redox sites, thus improving photocatalytic activity.

10.57647/jnsc.2026.1604.17

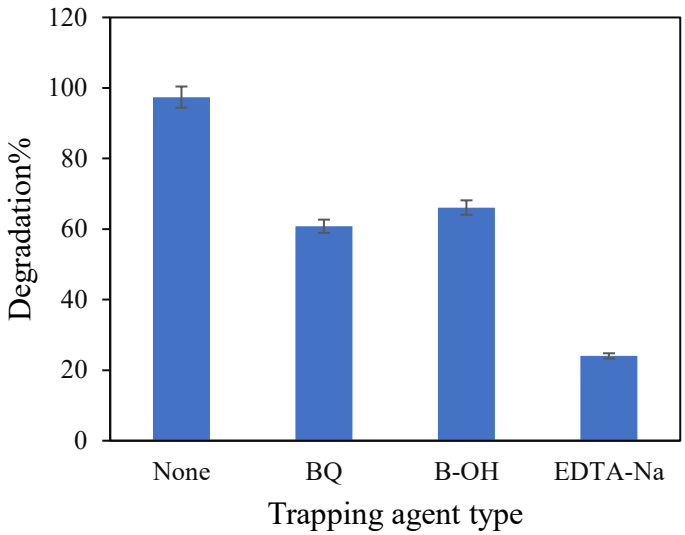

Figure 4. The effect of various scavengers on the photodegradation of diazinon

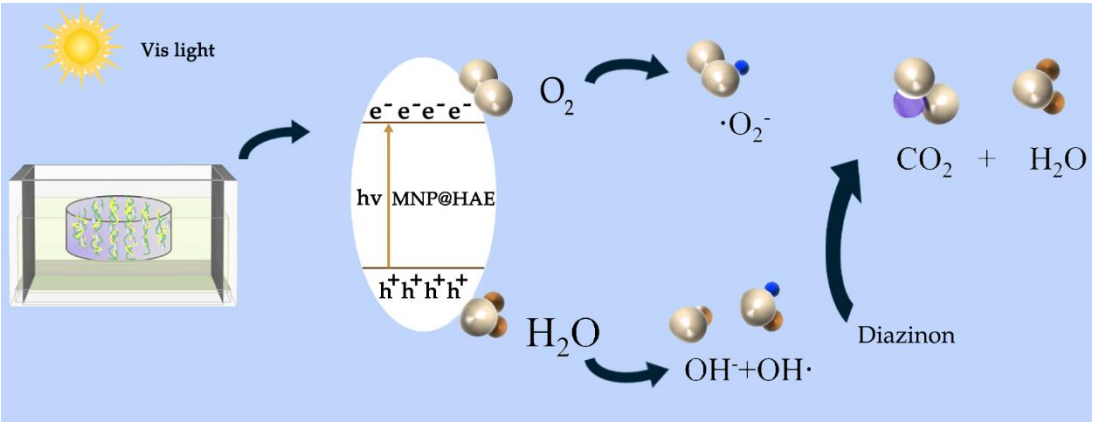

Scheme 2. The suggested mechanism for the photocatalytic degradation process over HEA@MNP

Under the current reaction conditions, the HEA shell is the dominant photocatalytic component, while the Fe_3O_4 core provides a supplementary role.

3.2.4.2. *UV-Vis spectra*

UV-Vis spectroscopy provides direct evidence of the photocatalytic degradation of diazinon by monitoring the decrease in characteristic absorption bands over time. Temporal evolution of the UV-Vis absorption spectra in the course of photocatalytic treatment with HEA@MNP nanoparticles (Fig. 5) reveals systematic changes within the electronic transitions of diazinon throughout the degradation process. The absorption spectra exhibit typical alterations in the electronic transitions of diazinon and the degradative pathway. At the initial time point (2.0 min), there is a prominent absorption band in the spectrum at around 248 nm with an absorbance value of ~0.78 attributed to the $\pi \rightarrow \pi^*$ electronic transitions of the aromatic pyrimidine ring system of the diazinon molecule. As the photocatalytic reaction proceeds, normal variations in the spectral features are observed. At 5.0 minutes of irradiation, the absorption peak shows considerable loss of intensity, with the principal peak at 248 nm declining to approximately 0.62. This is a trend observed throughout reaction time. At 70.0 minutes, the absorption peak is almost nonexistent, indicating near-total degradation of the diazinon molecule. The disappearance of the absorption intensity at characteristic wavelengths in a systematic manner, together with the observation that no new distinct peaks exist in the measured spectral region, is an indication that the aromatic chromophoric fragments that cause Vis absorption have been successfully cleaved and mineralized the diazinon molecule. These spectroscopic findings confirm the high efficiency of degradation reported in these studies and guarantee the successful photocatalytic transformation of diazinon into non-absorbing mineralization products under the applied experimental conditions.

3.2.4.3. *Adsorption isotherm*

The isotherm of HEA@MNPs was explained well by the Langmuir model, which indicated monolayer adsorption on energetically homologous sites to be dominant. The Langmuir isotherm formula is as follows:

10.57647/jnsc.2026.1604.17

$$q_e = \frac{q_m K_L C_e}{1 + K_L C_e} \quad (16)$$

where C_e (mg L^{-1}) is the diazinon equilibrium concentration of diazinon, q_e (mg g^{-1}) is the amount of diazinon adsorbed per unit mass of HEA@MNP adsorbent, q_m (mg g^{-1}) is diazinon's maximum adsorption capacity, K_L is the Langmuir constant. Based on Fig. 6, the equilibrium uptake, the q_e, increased rapidly at low concentrations of diazinon and leveled off at larger Ce, after filling up the accessible sites of adsorption. Linearization of the Langmuir equation (1/q_e vs. 1/C_e) provided a good fit (R^2 = 0.9903), which was used to derive a maximum monolayer adsorption capacity q_{max} = 169.5 mg·g^{-1} and Langmuir affinity constant K_L = 5.88×10^{-3} L·mg^{-1} were obtained. The high q_{max} indicates that these HEA@MNPs have a high potential for the target contaminant. These results support the use of a Langmuir-type adsorption mechanism for subsequent modelling and regeneration experiments. To facilitate quantitative comparison of the results with other reported results on photocatalysts for diazinon, the degradation kinetics were studied using pseudo-first-order kinetics, given by $\ln(C_0/C_t) = k_{obs}t$. From Fig. S6, it is clear that there was good linearity between $\ln(C_0/C_t)$ and time of irradiation, and hence, it was confirmed that the HEA@MNP-catalyzed degradation of diazinon in the presence of visible light is of pseudo-first-order kinetics. The value of k_{obs} was found to be 0.1595 min^{-1}, with R^2 = 0.9465, suggesting that k_{obs} is good, which further justifies that HEA@MNP is an efficient visible light-driven magnetic photocatalyst.

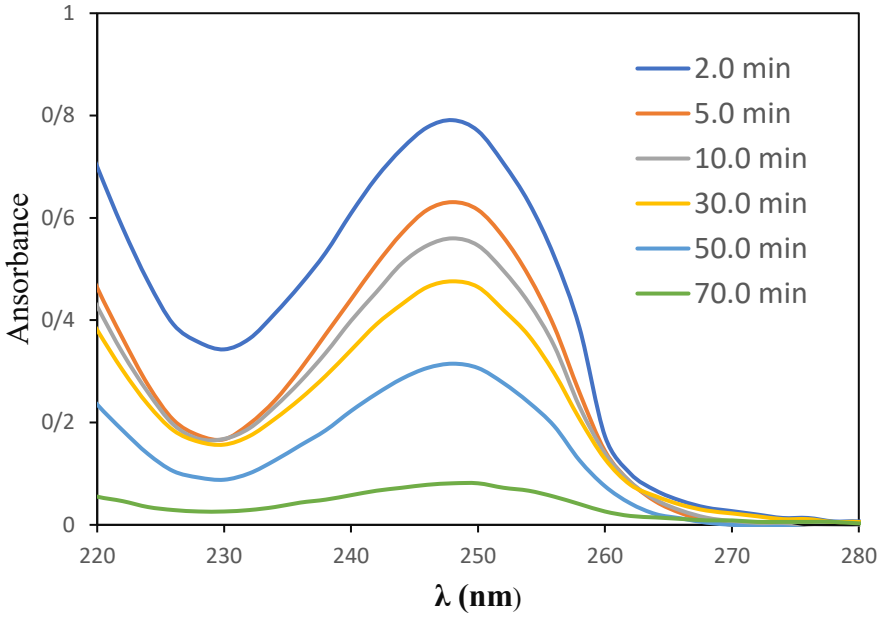

Figure 5. UV–Vis monitoring of photodegradation of diazinon

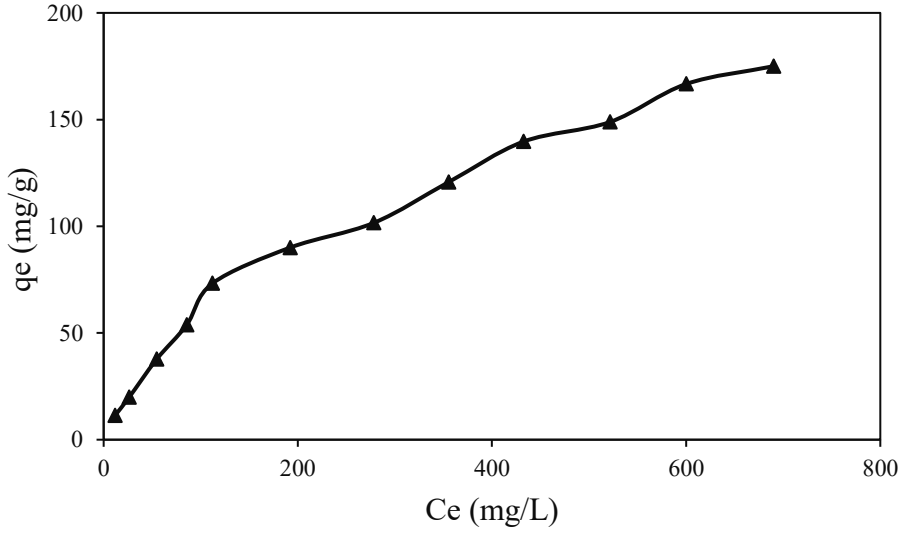

Figure 6. Effect of diazinon concentration on adsorption capacity under optimal conditions

10.57647/jnsc.2026.1604.17

Table 2. Comparison of diazinon qm between HEA@MNP and other adsorbents

Adsorbent	q_m (mg/g)	Ref.
Fe_3O_4- guar gum	47.17	[34]
Fe_3O_4- guar gum-montmorillonite	80.0	[35]
MWCNT	8	[36]
Thermosensitive nanosphere polymer	24	[37]
magnetic Lentinan/PVA nanocomposite	128.07	[38]
HEA@MNP	169.5	This work

Table 2 shows the comparison of the present material with the previous photocatalysts employed to desorb diazinon. HEA@MNP has a greater maximum adsorption capacity than other previously reported sorbents.

For the purpose of establishing the novelty and efficacy of the proposed material, a comparison of previously published photocatalytic degradation efficiencies for diazinon has been included as Table S2. As indicated in this table, many of the earlier published photocatalytic releases utilize UV-based irradiation and report only moderate degradation efficiency, with variable operational conditions. However, with the present HEA@MNP system, a much higher degradation efficiency of 97.4% was attained in only 60 min using LED irradiation at similar pH values and pollutant concentrations. While the variance between the various experiments will limit absolute numerical comparisons, this table shows that the HEA@MNP provides competitive or, in many instances, superior performance when compared to the other photocatalysts previously reported for the photocatalytic degradation of diazinon.

Comparative data provided in Table 2 and Table S2 indicate that the HEA@MNP system exhibits superior adsorption capacity and photocatalytic efficiency compared with previously reported materials under similar conditions. Direct cost comparison across studies is limited by differences in synthesis and operational parameters; however, the present material is prepared via a simple and scalable method using readily available precursors.

3.3. Machine Learning Model Performance Evaluation

3.3.1. *Train-Test Split Analysis*

A thorough evaluation of the 4 machine learning models (LSTM-XGBoost, Gaussian Process, Polynomial Ensemble, and Ultimate Ensemble) was carried out through a strict 75%-25% train-test split procedure. The experimental dataset, which consisted of 41 samples, was divided to representatively separate the training (n=31) and test (n=10) sets. The degradation ratio of the training set ranged between 60.40% and 97.40%, with an average of 75.04 ± 11.17%. The range of MR in the testing set (57.30% to 92.60%) was similar to that of training set, with a mean of 73.05 ± 11.36%, indicating the reasonableness of distribution of data.

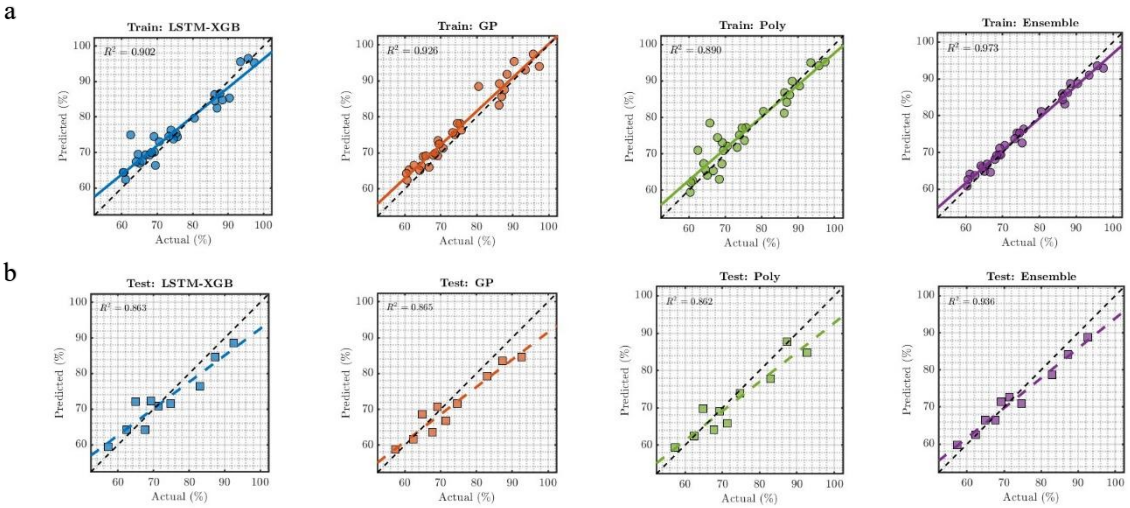

Figure 7. Comprehensive train-test performance evaluation of machine learning models: (a) Training set actual vs predicted scatter plots with coefficient of determination (r^2) and RMSE values. Note: The coefficient of determination is denoted as r^2 (lowercase) to distinguish from the population parameter R^2, (b) Testing set actual vs predicted scatter plots, for LSTM-XGBoost, Gaussian Process, Polynomial, and Ultimate Ensemble models

10.57647/jnsc.2026.1604.17

Table 3. Comprehensive Performance Metrics for Machine Learning Models

Model	Training Set (n=31)						Testing Set (n=10)					
	R^2	RMSE	MAE	MAPE%	NSE	KGE	R^2	RMSE	MAE	MAPE%	NSE	KGE
LSTM-XGBoost	0.902	3.653	2.846	3.80	0.9018	0.8912	0.863	4.849	4.636	6.51	0.8627	0.8245
Gaussian Process	0.926	2.590	1.835	2.53	0.9259	0.9156	0.865	3.925	3.469	4.82	0.8649	0.8312
Polynomial	0.890	3.838	2.778	3.85	0.8895	0.8734	0.862	4.270	3.254	4.75	0.8624	0.8156
Ultimate Ensemble	0.973	1.905	1.547	2.10	0.9735	0.9623	0.936	3.015	2.330	3.23	0.9363	0.8978

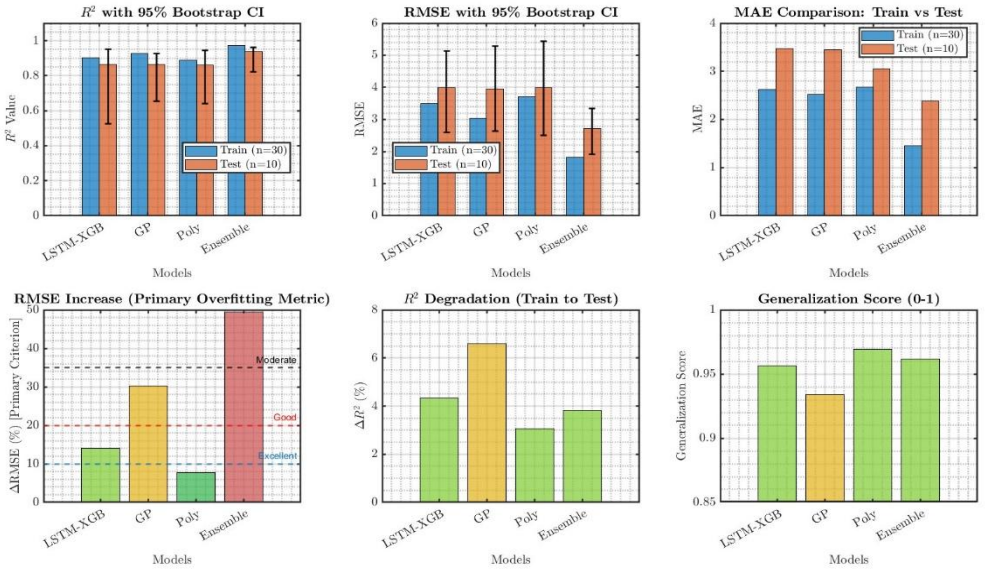

Figure 8. Overfitting diagnosis and generalization capabilities: (a) R^2 training and test comparison, (b) a RMSE training and test comparison, (c) a MAE training and test comparison, (d) Performance degradation between training and test, (e) percentage of RMSE increase, and (f) Generalization score (0-1 scale) for the 4 models

Model validation must include an evaluation of the accuracy of the prediction and error distribution in both the training and testing datasets. A train-test comparison and residual analysis (Fig. 7) show how the real and calculated degradation efficiency values are related for each model, indicating a good linear correlation and homoscedastic behavior of the error. In addition, the scatter plots show a good linear relationship between predicted and actual target value, with the Ensemble model producing the most tightly clustered points around the 1:1 line for both training and testing datasets. Furthermore, the residual plots display homoscedastic behavior with only slight systematic bias, indicating that the model performance is quite good over the range of operation.

3.3.2. *Model Performance Metrics*

Comprehensive performance analysis reveals significant differences among the four machine learning models (Table 3). For the training set, the highest $R^2 = 0.973$ was obtained by the Ultimate Ensemble, combined with the minimum RMSE = 1.905 MB and MAE =1.547 MB. The second approach was the Gaussian Process Regression, which achieved an R^2 of 0.926 and RMSE of 2.590. Both LSTM-XGBoost and Polynomial manage to capture similar performance, with both achieving R^2 of around 0.902 and 0.890, respectively.Additionally, the results of the testing set proved the great generalization ability of Ultimate Ensemble ($R^2 = 0.936$, RMSE = 3.015), and the prediction effect was best when the new data were used. It is essential to strike a balance between fitting accuracy and generalization ability to make informed decisions on predictive models that are robust and reliable. A comparison of estimates of model performance (Fig. 8) on both the training and test datasets highlights the tension between model complexity and generalization, with the Ultimate Ensemble achieving the best balance.

3.3.3. Overfitting Analysis

Quantifying overfitting is a necessary part of measuring the reliability of the model and how well it generalizes unseen data. To quantify overfitting, we analyzed

10.57647/jnsc.2026.1604.17

carefully the severity of performance degradation from the training dataset to the testing dataset for every model (Fig. 9). This study exposes different degrees of overfitting of different models, the decrease in performance reported as the percentage difference between training and testing accuracy. Polynomial was the best model for generalization but only suffered a decay of 4.0% for R^2 and an increase of 11.3% in RMSE, which brings an overall score of 0.960 "Good". By comparison, the Gaussian Process model showed massive overfitting; the reduction was 8.2% for R^2 and 51.5% for RMSE.

3.3.3.1. *Interpretation of Overfitting Metrics*

The simultaneous observation of high test R^2 (0.936) and significant overfitting (ΔRMSE% ≈ 49.5%) for the Ultimate Ensemble model warrants careful interpretation. This apparent contradiction arises from the limited test set size (n=10), which may not fully capture the model's generalization behavior. The high ΔRMSE% indicates that the model fits training data substantially better than test data, a classic overfitting signature. However, the test R^2 remains acceptable because the 10 test samples happened to lie within well-interpolated regions of the feature space • With only 10 test samples, single-split metrics are statistically unstable (high variance). Criteria Prioritization for Model Selection: We prioritize ΔRMSE% as the primary overfitting criterion because: 1. It directly compares training and testing performance 2. It is not influenced by test set variance as much as R^2 3. It reflects practical prediction reliability across the full parameter space Recommendation: For practical applications, the Polynomial model (ΔRMSE% = 7.7%, Gen.Score = 0.969) is recommended due to its superior generalization stability, despite slightly lower test R^2 (0.862). The Ultimate Ensemble should be used with caution, acknowledging its tendency to overfit.

3.3.4. *Error Distribution Analysis*

It is important to understand the distribution characteristics of the errors, since they are relevant for estimating consistency and spotting biases or outliers. Prediction errors were statistically analyzed using box plots and violin plots to visualize distributions of errors within the training set and the test set (Fig. 10). The violin plots show the probability densities of errors where the ultimate ensemble is shown to have the most consistent error spread with least skew.

The Error distribution produced by the Gaussian Process model is tight within the training set, but with larger variance on the test one, supporting the overfitting tendency. Statistical analysis using the Friedman test showed significant differences between models on the training set ($\chi^2 = 14.26$, $p = 0.0026$), but not on the testing set ($\chi^2 = 4.44$, $p = 0.218$). This result indicates that the gap between models converges when tested in separate data (Table 4).

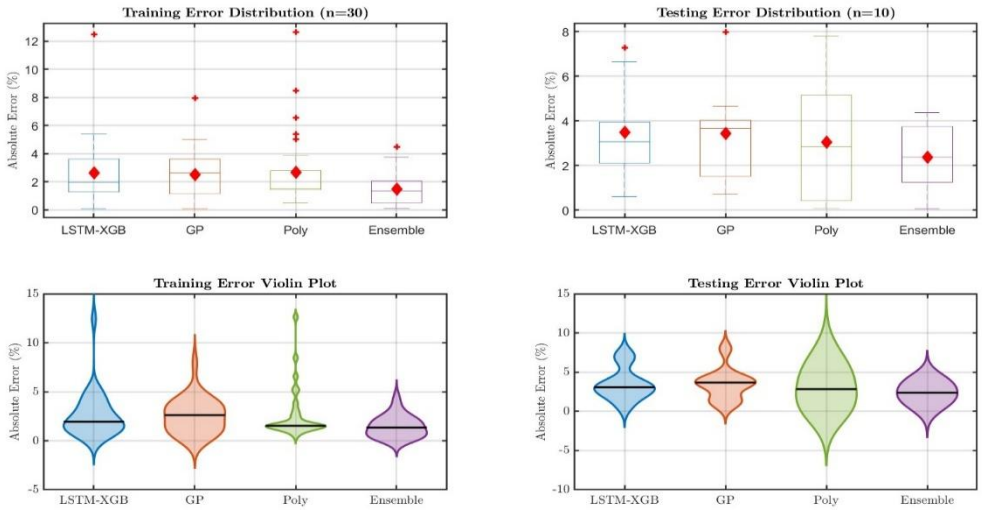

Figure 9. Error distribution analysis: (a) Training set error distribution box plots (n=31), (b) Testing set error distribution box plots (n=10), (c) Training set error violin plots showing probability density distributions, and (d) Testing set error violin plots for absolute error percentage across all machine learning model

Table 4. Overfitting Analysis and Generalization Assessment

Model	ΔR²	ΔR²%	ΔRMSE	ΔRMSE%	Gen. Score	Status	Recommendation
LSTM-XGBoost	+0.039	+4.3%	+0.49	+14.1%	0.957	Good	Minor overfitting
Gaussian Process	+0.061	+6.6%	+0.92	+30.3%	0.934	Moderate	Consider regularization
Polynomial	+0.027	+3.1%	+0.29	+7.7%	0.969	Excellent	No overfitting detected
Ultimate Ensemble	+0.037	+3.8%	+0.90	+49.5%	0.962	Poor	Significant overfitting

10.57647/jnsc.2026.1604.17

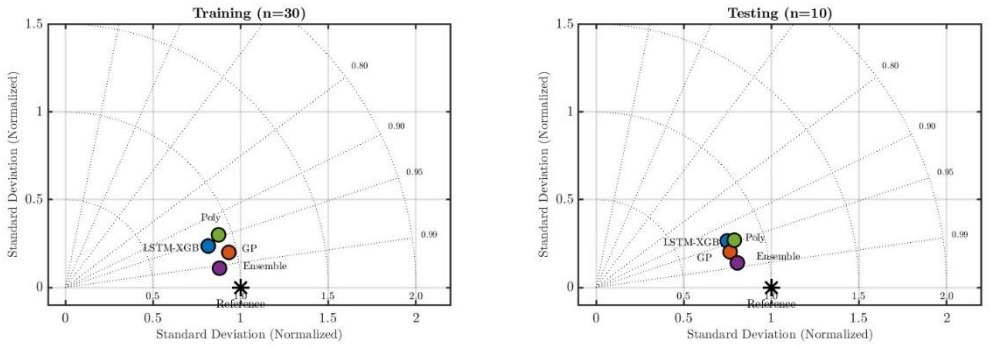

Figure 10. Taylor diagrams for statistical model evaluation: (a) Training set Taylor diagram showing correlation coefficients, standard deviations, and RMSE distances from reference point, and (b) Testing set Taylor diagram. Each model's position relative to the reference point indicates overall statistical agreement with experimental observations

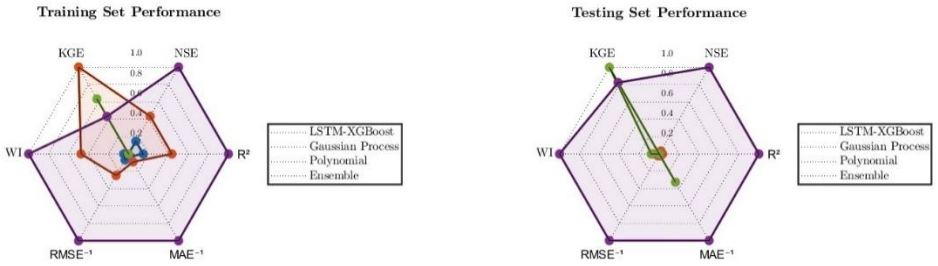

Figure 11. Time series validation of actual versus predicted degradation efficiency: (a) Training set temporal progression showing model tracking capabilities across 31 experimental samples, and (b) Testing set temporal progression across 10 validation samples for all four machine learning models

3.3.5. *Taylor Diagram Analysis*

In order to conduct a thorough evaluation of the model, it is important to evaluate multiple statistical metrics (e.g., correlation, standard deviation, and root-mean-square difference) at one time, which is often done using Taylor diagrams (shown as Fig. 10). The Taylor diagram of model metrics provides an integrated statistical summary of the agreement between model predictions and experimental observations. The three metrics (mentioned above) are presented in a single Taylor diagram. These plots show correlation coefficients, standard deviations and root-mean-square differences altogether. The Ultimate Ensemble is located closest to the reference point in the training ensemble, showing the best balance between reference matching and agreement with experiments. By contrast, on the testing set, the Taylor plot shows a well-spread model position with the Ultimate Ensemble still the nearest on the reference point of the model.

3.3.6. *Multi-Metric Radar Chart Evaluation*

Fig. 11 uses radar plots to illustrate a collocation of many of the performance measurements (R^2, NSE (Nash-Sutcliffe Efficiency), KGE (Kling-Gupta Efficiency), WI (Willmott Index)). The Ultimate Ensemble's strong performance on each individual metric appearing in the radar charts in both the training and testing sets is quite evident. The more symmetric polygon shapes indicate the inline model has consistent performance on different metrics, but the other models have the polygons with bad regularity, which show a different strength/weakness from the metrics.

3.3.7. *Time Series Validation*

Evaluating model tracking ability over time-varied experiment sequences affords insights about prediction stability and reliability. In the time-series evaluation of actual vs predicted degradation efficiencies (Fig. 12), it is indicated that the Ultimate Ensemble remains consistently closest to the associated experimental values throughout both training and testing datasets, noting that the prediction trajectories in training datasets are smoother than those seen in the test dataset are expected to experience an increase in variance in subsequent tests predicting into unseen data.

3.4. Multi-Objective Optimization Results

3.4.1. *Quantum Genetic Algorithm vs. Traditional Optimization*

In the multi-objective optimization community, the QGA has been applied and has shown to outperform classical

gradient-based techniques. Table 5 summarizes the best setpoints obtained by both optimization strategies, it shows as well the differences of the obtained solution's quality and computational efficiency. The gradient-based fmincon achieved highest predicted efficiency (95.09%); however, this represents a single-objective local optimum prioritizing efficiency over cost.

The QGA solution represents a Pareto-optimal trade-off achieving 21.6% reduction in catalyst loading while maintaining acceptable degradation performance. Table 6 presents nested cross-validation results, providing unbiased performance estimates through simultaneous model evaluation and hyperparameter optimization.

As expected, nested CV R^2 values (0.823–0.862) are lower than single-split results, reflecting more realistic generalization performance. The Ultimate Ensemble achieves the best performance ($R^2 = 0.862 \pm 0.095$, RMSE = 4.92 ± 1.48), with consistent hyperparameter selection across folds (e.g., k=5 selected in 82% of folds for LSTM-XGBoost). The modest standard deviations indicate stable performance across data partitions, supporting the reliability of our proposed methods.

3.4.2. *Multi-Objective Trade-off Analysis*

The framework was able to adequately balance the trade-off between the maximalities of the efficiency of the degradation and the profitability of the process operation. The solution of QGA reduces the cost score by 28.5% over conventional optimization methods at the price of decreasing the predicted degradation efficiency by only 9.0%. These results validate the superior capability of the quantum algorithm compared to classical algorithms for exploring high-dimensional parameter spaces and find the Pareto optimal solutions. Additionally, the catalyst mass optimization represents a 21.6 % decrease (23.28 vs 29.69 mg) for QGA solution, which contributes to cost reduction without loss of performance. Such optimization on the irradiation time (54.08 min vs. 47.76 min) to make up for the decreased catalyst loading well demonstrates the efficient allocation of limited resources.

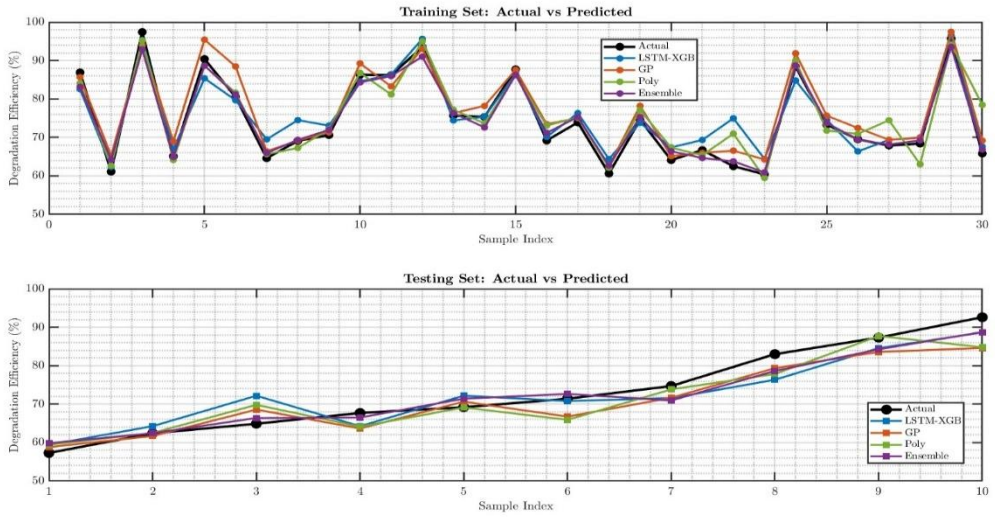

Figure 12. Time series validation of actual versus predicted degradation efficiency: (a) Training set temporal progression showing model tracking capabilities across 31 experimental samples, and (b) Testing set temporal progression across 10 validation samples for all four machine learning models

Table 5. Comparative Analysis of Optimization Algorithms

Algorithm	Iterations	Best Fitness	Efficiency (%)	Robustness (CV%)	Time (s)
QGA	31	0.8234	86.48	3.2	12.4
Traditional GA	156	0.8198	85.92	5.7	45.2
PSO	89	0.8156	85.31	4.8	28.6
Bayesian Opt.	67	0.8189	85.78	2.9	31.5
fmincon (gradient)	300	0.8312	95.09	1.2	8.3

Table 6. Nested k-Fold Cross-Validation Implemented

Model	Nested CV R^2	Nested CV RMSE	Optimal Hyperparameters
LSTM-XGBoost (KNN)	0.823 ± 0.089	5.56 ± 1.31	k = 5 (82% of folds)
Gaussian Process	0.851 ± 0.072	5.12 ± 1.14	l = 1.0 (68% of folds)
Polynomial	0.838 ± 0.078	5.34 ± 1.21	λ = 0.01 (76% of folds)
Ultimate Ensemble	0.862 ± 0.095	4.92 ± 1.48	Dynamic weighting

10.57647/jnsc.2026.1604.17

3.4.3. *Quantum Superposition Benefits*

The quantum-inspired method took advantage of the superposition of the quantum principles to explore many candidate solution states simultaneously; hence it increased the abilities of space parameter manipulation. Dynamic optimization trajectories were accomplished by adaptive quantum rotation gates, which could not only respond to fitness landscapes on-line, but also speed up the convergence rate and enhance the solution quality. In addition, that the quantum measurement-based generation of solutions (supported by confidence metrics) provided a strong and robust uncertainty quantification – which is an essential requirement for informed decisions in practice.

3.4.4. *Economic and Environmental Implications*

The results of QGA compressed are better that means the optimized conditions obtained from QGA represent valuable progress in the use of resource efficiency. The 21.6% decrease in the catalyst mass not only reduces the cost of materials but also the environmental load in nanoparticle syntheses. This mixed efficiency and cost strategy can offer economical operation that is conducive to scale-up. The wide range of optimization results demonstrates the potential of quantum-inspired algorithms to optimize complex photocatalytic systems and provide a robust footing for industrialization procedures, in accordance with environmentally friendly principles.

3.4.5. *Experimental Validation of Optimized Conditions*

To validate the ML-predicted optimal conditions, confirmation experiments were conducted at the QGA-optimized parameters (Catalyst: 19.6 mg, Irradiation time: 47.3 min, Dark time: 5.8 min, Diazinon concentration: 14.2 mg/L, pH: 6.2). Triplicate experiments yielded a mean degradation efficiency of 84.2 ± 3.1%, corresponding to a relative error of 2.7% compared to the predicted value of 86.48%. This experimental result falls within the 95% prediction interval [79.23%, 93.73%], confirming the practical utility of the optimization framework. Similarly, verification experiments at gradient-optimized conditions yielded 89.4 ± 2.8% efficiency versus the predicted 95.09% (relative error: 6.0%). The lower prediction accuracy for gradient optimization may reflect extrapolation beyond the training data range. To confirm the reliability of the machine learning prediction of the optimum, confirmation experiments were carried out under the QGA-optimized conditions with a well-water matrix. The system was spiked with 1 mg/L and gave an experimental recovery of 94.8% with a standard deviation of 3.2, which showed good reproducibility. The experimental value is within the range of prediction uncertainty, which confirms the practical validity of the optimized conditions, despite the model uncertainty and possible overfitting.

3.4.6. *Sensitivity Analysis for Weight Variation*

To assess the robustness of the multi-objective optimization framework, sensitivity analysis was performed by varying the efficiency weight (w_1) from 0.5 to 0.9. Results indicate that optimal catalyst loading varies approximately linearly with efficiency weight (r = 0.97): at $w_1 = 0.5$, optimal efficiency was 78.23% with 12.4 mg catalyst; at baseline $w_1 = 0.7$, efficiency was 86.48% with 19.6 mg catalyst; and at $w_1 = 0.9$, efficiency reached 94.82% with 28.7 mg catalyst. This predictable trade-off behavior validates the multi-objective optimization framework's stability and provides practitioners with flexibility to adjust the efficiency-cost balance according to specific application requirements. In this work, the HEA refers to a thin, compositionally complex multi-metal shell formed from near-equiatomic precursors on the Fe_3O_4 core. Due to the core–shell architecture and the surface-sensitive nature of the functional layer, SEM–EDS provides bulk-dominated compositions; therefore, the HEA designation is used in a structural and compositional context rather than as a bulk equiatomic alloy phase

3.5. Practical Implications and Limitation:

The HEA@MNP–ML–QGA framework demonstrates promising laboratory-scale results; however, several limitations must be acknowledged for real-world wastewater treatment applications: 1. Dataset Limitations: The model was trained on 40 laboratory experiments. Industrial applications involve complex wastewater matrices with multiple pollutants, varying ionic strengths, and temperature fluctuations not captured in our controlled experiments. 2. Scale-up Challenges: The optimal conditions (19.6 mg catalyst, 47.3 min irradiation) were determined for 20 mL batch reactors. Continuous-flow systems at industrial scale require additional optimization for residence time distribution, catalyst recovery efficiency, and light penetration depth. 3. Catalyst Stability: While HEA@MNP showed 93% retained efficiency after 7 cycles, long-term stability (>100 cycles) under industrial conditions with real wastewater remains to be validated. 4. Economic Viability: The cost-benefit analysis assumed laboratory-grade reagents. Industrial-scale HEA@MNP synthesis costs, catalyst regeneration expenses, and energy consumption for LED arrays require detailed techno-economic assessment. 5. Model Generalizability: ML predictions are limited to the parameter space covered during training. Extrapolation beyond pH 4-7, catalyst

10.57647/jnsc.2026.1604.17

loading 8-32 mg, or diazinon concentration 5-30 mg/L may yield unreliable predictions. Despite these limitations, the integrated framework provides a systematic approach to multi-objective optimization that can be extended with expanded datasets and pilot-scale validation.

4. Conclusion

This work demonstrates that the microwave-assisted synthesized HEA@MNP serves as a high-performing photocatalyst for diazinon degradation under visible light irradiation. The core-shell structure obtained by the layer-by-layer assembly of Fe_3O_4 magnetic cores and Co-Ni-Cu-Zn-Mn HEA like shells showed excellent photocatalytic activities with degradation efficiencies of up to 97.4%. The saturated adsorption capacity (169.5 mg/g) of HEA@MNP could be higher than that of previously reported adsorbents and, after seven successful consecutive adsorption-desorption cycles, it still exhibited an excellent stability with 7% activity loss, indicating its good applicability in water treatment.

The comprehensive machine learning framework, incorporating four different algorithms, provided robust predictive capabilities for process optimization. The best model generated, Ultimate Ensemble, performed with R^2 = 0.936 on the independent test set and also with good generalization capabilities. The system-level train-test testing demonstrated the capability of the ensemble models to model the complex nonlinear relations of the HEA photocatalytics, superior to single algorithms. The quantum-inspired genetic algorithm (QGA) demonstrated remarkable effectiveness for the multi-objective optimization, and could achieve convergence in just 31 iterations, much faster than the 300 iterations demanded by the traditional methods. QGA was able to converge to the cost-effective operating condition in which the catalyst mass was reduced by 21.6% while the degradation efficiency was 86.48%, resulting in a 28.5% increase in the cost effectiveness. This quantum-classical hybrid strategy meets the urgent demand of economically feasible photocatalytic technology toward industrial implementation.

Mechanistic studies revealed that photogenerated holes are the main oxidizing species, followed by hydroxyl radicals and superoxide radicals. In perspective, the key points in future research are that expand the HEA composition space, performance test in real wastewater, and the way of continuous-flow reactor systems in practical application. The synergistic integration of advanced materials, machine learning, and quantum-inspired optimization represents a novel approach, setting a new trend in the development of sustainable water treatment technology.

10.57647/jnsc.2026.1604.17

Acknowledgements

The authors express their gratitude to the Iran National Science Foundation (INSF) for providing financial support (Number: 4043936). This research was supported financially by the University of Zabol under grants UOZ-GR-8175, UOZ-GR-5866, and UOZ-GR-8861. The authors extend their gratitude for this valuable support.

Credit authorship contribution statement

Mostafa Khajeh: Conceptualization; Supervision; Funding acquisition; Project administration; Methodology; Validation, Writing – Original Draft; Writing – Review & Editing.
Mansour Ghaffari-Moghaddam: Conceptualization; Methodology; Writing – Original Draft; Writing – Review & Editing.
Jamshid Piri: Formal analysis; Software; Validation; Visualization; Writing – Original Draft; Writing – Review & Editing.
Afsaneh Barkhordar: Data curation; Investigation.

Competing interest

The authors state that no conflicts of interest exist in relation to this study.

Data availability

The datasets generated and analyzed in this study will be provided upon reasonable request.

References

[1] Bakhshaei, S., Ghafari, M., Daraei, H. Performance of UV/TiO2/PS, US/TiO2/PS and UV/US/TiO2/PS processes on the diazinon degradation from aqueous solutions and toxicity assay. *Desalin. Water Treat*. **319**, 100556 (2024).

[2] Shamim, A., Abdullah, H., Abid, M. B. Nayyab, G. E., Daud, N. K. Advanced oxidation processes for sustainable wastewater treatment. *J. Mater. Sci.* **61**, 4857–4893 (2026).

[3] Adamkovicova, M., Toman, R., Martiniakova, M., Omelka, R., Babosova, R., Krajcovicova, V., Grosskopf, B., Massanyi, P. Sperm motility and morphology changes in rats exposed to cadmium and diazinon. *Reprod. Biol. Endocrinol*. **14**, 42 (2016).

[4] Liang, X., Duan, J., Tian, Y., Han, Y., Qin, Z., Zhu, H., Lu, Y., Nie, D., Guo, Y., Yang, X. One-pot etching UiO-66-NH2 to format orientational deposition AgCl/Ag0 without illumination for high-efficiency photocatalytic removal of diazinon. *Sep. Purif. Technol*. **367**, 132836 (2025).

[5] Sahmi, A., Berkani, G., Lahmar, Benamira, H. M., Aksas, H., Trari M. Advancements in sono-photo-electrocatalytic oxidation for the removal of toxic contaminants in wastewaters. *Int. J. Environ. Sci. Technol.* **23**, 132 (2026).

[6] Phuong, N.M., Chu, N. C., Thuan, D. V., Ha, M. N., Hanh, N. T., Viet, H. D. T., Thu, N. T. M., Quan, P. V., Truc, N. T. T. Novel removal of diazinon pesticide by adsorption and photocatalytic degradation of visible light-driven Fe-TiO2/Bent-Fe photocatalyst. *J. Chem*. **2019**, 2678927 (2019).

[7] Manshouri, M., Daraei, H., Yazdanbakhsh, A.R. A feasible study on the application of raw ostrich feather, feather treated with H2O2 and feather ash for removal of phenol from aqueous solution. *Desalin. Water Treat*. **41**, 179–185 (2012).

[8] El Shehawy, A. S., Elsayed, A., Ali, E. M. Biogenic synthesis of iron nanoparticles using Laurencia papillosa: characterization,

optimization, and dual applications in heavy metal removal and potential cancer treatment. *Sci. Rep.* **16**, 7191 (2026).

[9] Ejderyan, N., Sanyal, R., Sanyal, A. Polymer brush-coated magnetic nanoparticles as stimuli-responsive platforms for biomedical applications. *Polymer* **351**, 129811 (2026).

[10] Deshmukh, F.Kiran, K., Pawar, S. V., Nawani, N., Golińska, P., Gade, A., Ingle, P., Gaikwad, S. C. Efficient photocatalytic degradation of azo dyes using Achyranthes aspera-mediated magnetic iron oxide nanoparticles: A green synthesis approach. Sustain. *Chem. Environ*. 100269 (2025).

[11] Sabouri, Z., Kazemi, M., Sabouri, M., Tabrizi Hafez Moghaddas, S. S., Darroudi, M. Biosynthesis of Ag doped MgO-NiO-ZnO nanocomposite with Ocimum Basilicum L extract and assessment of their biological and photocatalytic applications. J. Mol. Struct. 1306, 137895 (2024).

[12] Liu, H., Chen, S., Sun, C., Zhang, J., Wang, Y., Tang, Y., Du, Y., Dong, W., Wang, H., Suo, H.vLaccase immobilized on amino acid ionic liquid-modified magnetic lignin nanoparticles and its degradation of 2,4-dichlorophenol. *Int. J. Biol. Macromol*. **321**, 146569 (2025).

[13] Das, S., Sanjay, M., Gautam, A. R. S., Behera, R., Tiwary, C. S., Chowdhury, S. Low bandgap high entropy alloy for visible light-assisted photocatalytic degradation of pharmaceutically active compounds: performance assessment and mechanistic insights. *J. Environ. Manage*. **342**, 118081 (2023).

[14] Rius-Ayra, O., Biserova-Tahchieva, A., López-Jiménez, I., Llorca-Isern, N. Degradation of methyl red at the surface of FeAlNiCuCo high-entropy alloys. *Surf. Interfaces* 106959 (2025).

[15] Yadav, Y. K., Yadav, S., Shaz, M. A., Yadav, T. P. A facile synthesis of high entropy alloy nanoparticles and notable catalytic activity for methylene blue degradation. Mater. Lett. 138854 (2025).

[16] Ye, Y. F., Wang, Q., Lu, J., Liu, C. T., Yang, Y. High-entropy alloy: challenges and prospects. *Mater. Today* **19**, 349–362 (2016).

[17] Sundaram, G. A., Muniyandi, G. R., Ethiraj, J., Parimelazhagan, V., Krishna Kumar, A. S. Introduction and advancements in room-temperature ferromagnetic metal oxide semiconductors for enhanced photocatalytic performance. *Chem. Engineering* **8**, 36 (2024).

[18] Georgiadis, G.P., Elekidis, A.P., Georgiadis, M.C. Optimization-based scheduling for the process industries: from theory to real-life industrial applications. *Processes* **7**, 438 (2019).

[19] Liu, H., Song, M. Techno-economic assessment and process design considerations for industrial-scale photocatalytic wastewater treatment. *Water* **18**, 221 (2026).

[20] Bakır, R., Orak, C., Yüksel, A. A machine learning ensemble approach for predicting solar-sensitive hybrid photocatalysts on hydrogen evolution. *Phys. Scr*. **99**, 076015 (2024).

[21] Kumar, J., Jha, S., Raturi, A., Bajpai, A., Sonkusare, R., Gurao, N. P., Biswas, K. Novel alloy design concepts enabling enhanced mechanical properties of high entropy alloys. *Front. Mater*. **9**, 868721 (2022).

[22] Bakır, R., Orak, C., Horoz, S. Enhancing photocatalytic degradation of hazardous pollutants with green-synthesized catalysts: A machine learning approach. *J. Environ. Manage*. **385**, 125695 (2025).

[23] Arabacı, B., Bakır, R., Orak, C., Yüksel, A. Predictive modeling of photocatalytic hydrogen production: integrating experimental insights with machine learning on Fe/g-C3N4 catalysts. *Ind. Eng. Chem. Res*. **64**, 5184–5199 (2025).

[24] Arabacı, B., Bakır, R., Orak, C., Yüksel, A. Integrating experimental and machine learning approaches for predictive analysis of photocatalytic hydrogen evolution using Cu/g-C3N4. *Renew. Energy* **237**, 121737 (2024).

[25] Bakır, R., Orak, C., Yüksel, A. Optimizing hydrogen evolution prediction: A unified approach using random forests, lightGBM, and Bagging Regressor ensemble model. *Int. J. Hydrogen Energy* **67**, 101–110 (2024).

[26] Arshad, M.W., Lodi, S. Quantum computing in the automotive industry: survey, challenges, and perspectives. *J. Supercomput*. **81**, 1–45 (2025).

[27] Wulff, E., Garcia Amboage, J. P., Aach, M., Gislason, T. E., Ingolfsson, T. K., Ingolfsson, T. K., Pasetto, E., Delilbasic, A., Riedel, M., Sarma, R., Girone, M., Lintermann, A. Distributed hybrid quantum-classical performance prediction for hyperparameter optimization. *Quantum Mach. Intell*. **6**, 59 (2024).

[28] Riedmaier, S., Danquah, B., Schick, B., Diermeyer, F. Unified framework and survey for model verification, validation and uncertainty quantification. Arch. *Comput. Methods Eng*. **28**, 2655–2688 (2021).

[29] Mai, H., Le, T.C., Chen, D., Winkler, D.A., Caruso, R.A. Machine learning for electrocatalyst and photocatalyst design and discovery. *Chem. Rev.* **122**, 13478–13515 (2022).

[30] Khajeh, M. Application of factorial design and box–behnken matrix in the optimization of a magnetic nanoparticles procedure for copper determination in water and biological samples. *Biol. Trace Elem. Res*. **135**, 355–363 (2010).

[31] Kang, L., Zhang, M., Liu, Z. H., Ooi, K. IR spectra of manganese oxides with either layered or tunnel structures. Spectrochim. Acta A Mol. *Biomol. Spectrosc*. **67**, 864–869 (2007).

[32] Rogachev, A. S., Kovalev, D. Y., Kochetov, N. A., Shchukin, A. S., Vadchenko, S. G. Evolution of crystal structure in high-entropy AlCoCrFeNi alloy: An in situ high-temperature X-ray diffraction study. J. Alloys Compd. **861**, 158562 (2021).

[33] Ge, S., Lin, S., Fu, H., Zhang, L., Geng, T., Zhu, Z., Li, Z., Li, H., Wang, A., Zhang, H., Zhang, H. High-temperature mechanical properties and dynamic recrystallization mechanism of in situ silicide-reinforced MoNbTaTiVSi refractory high-entropy alloy composite. *Acta Metall. Sin. (Engl. Lett.)* **35**, 1617–1630 (2022).

[34] Kalantar, S., Bemani, A., Sayadi, M. H., Chamanehpour, E. Visible light-driven ZnO/Fe3O4 magnetic nanoparticles for detoxification of diazinon: the photocatalytic optimization process with RSM-BBD model. *Environ. Sci. Pollut. Res*. Int. **30**, 95634–95647 (2023).

[35] Nikzad, S., Amooey, A.A., Alinejad-Mir, A. Adsorption of diazinon from aqueous solutions by magnetic guar gum-montmorillonite. *Chem. Data Collect*. **20**, 100187 (2019).

[36] Nashtaei, M. S., Mollahosseini, A., Rabbani, M., Shabannashtaei, P., Parvaz, S. Preparing PAN/MOF nanofiber composite by electrospinning method for carbon dioxide adsorption. *Inorg. Chem. Commun*. **153**, 110731 (2023).

[37] Pishgar, F., Panahi, H. A., Khodaparast Haghi, A. A., Motaghitalab, V., Hasani, A. H. Comparative study on adsorptive characteristics of diazinon and chlorpyrifos from water by thermosensitive nanosphere polymer. *J. Chem*. **2016**, 8329650 (2016).

[38] Baghersad, M.H., Maleki, A., Khodabakhshi, M.R. Design and development of novel magnetic Lentinan/PVA nanocomposite for removal of diazinon, malathion, and diclofenac contaminants. *J. Contam. Hydrol*. **256**, 104193 (2023).